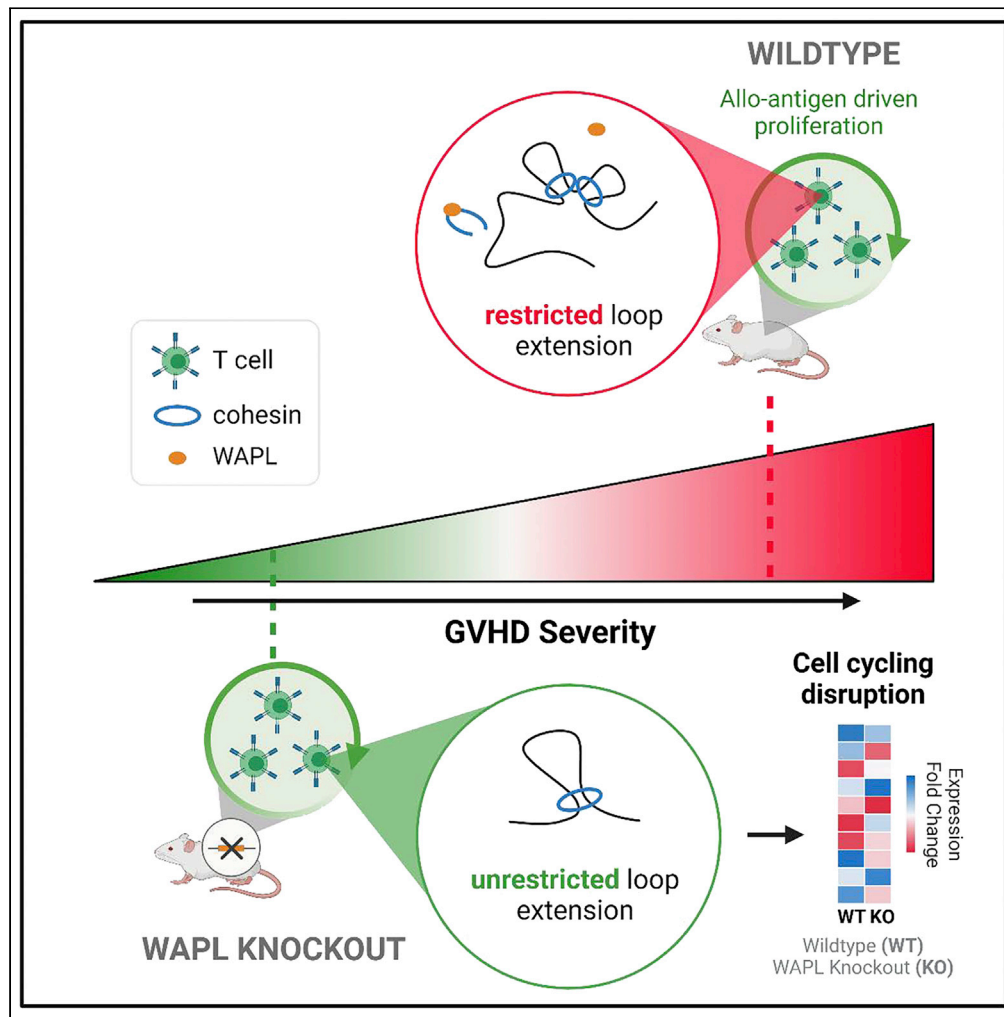


Article

Rearrangement of T Cell genome architecture regulates GVHD



Yaping Sun,
Gabrielle A.
Dotson, Lindsey A.
Muir, ..., Walter
Meixner, Indika
Rajapakse, Pavan
Reddy

reddypr@med.umich.edu

Highlights

WAPL regulates
chromatin loop extension
in T cells

WAPL depletion disrupts
cell cycling of T cells

WAPL deletion regulates
allogeneic T cell
responses and GVHD



Article

Rearrangement of T Cell genome architecture regulates GVHD

Yaping Sun,^{1,4} Gabrielle A. Dotson,^{2,4} Lindsey A. Muir,² Scott Ronquist,² Katherine Oravec-Wilson,¹ Daniel Peltier,¹ Keisuke Seike,¹ Lu Li,¹ Walter Meixner,² Indika Rajapakse,^{2,3} and Pavan Reddy^{1,5,*}

SUMMARY

WAPL, cohesin's DNA release factor, regulates three-dimensional (3D) chromatin architecture. The 3D chromatin structure and its relevance to mature T cell functions is not well understood. We show that *in vivo* lymphopenic expansion, and alloantigen-driven proliferation, alters the 3D structure and function of the genome in mature T cells. Conditional deletion of WAPL, cohesin's DNA release factor, in T cells reduced long-range genomic interactions and altered chromatin A/B compartments and interactions within topologically associating domains (TADs) of the chromatin in T cells at baseline. WAPL deficiency in T cells reduced loop extensions, changed expression of cell cycling genes and reduced proliferation following *in vitro* and *in vivo* stimulation, and reduced severity of graft-versus-host disease (GVHD) following experimental allogeneic hematopoietic stem cell transplantation. These data collectively characterize 3D genomic architecture of T cells *in vivo* and demonstrate biological and clinical implications for its disruption by cohesin release factor WAPL.

INTRODUCTION

The three-dimensional (3D) architecture of the genome includes coiling of genomic DNA around histone proteins to form the chromatin fiber, which folds into higher-order structures such as loops, domains, compartments, and chromosomes (Bonev and Cavalli, 2016; Finn and Misteli, 2019; Misteli, 2020; Rajapakse et al., 2011; Rajapakse and Groudine, 2011). High-resolution chromatin conformation capture experiments reveal that the 3D spatial architecture of the chromatin at various scales is conserved, reproducible at the cellular level, and regulates gene expression (Cremer and Cremer, 2001, 2019; Dekker and Mirny, 2016; Dekker et al., 2002). It is increasingly appreciated that higher spatial organization can have specific alterations during mammalian development and in some pathologies including cancers and infections (Finn and Misteli, 2019; Waldman, 2020). However, whether a *priori* disruption of this 3D organization alters *in vivo* cellular functions and disease processes remains poorly understood.

The multi-unit cohesin ring complex plays a critical role in 3D genomic organization and in cell division. It consists of SMC1/3, SCC1 (RAD21), and STAG subunits that are loaded by the SCC2/SCC4 complex onto genomic DNA and establish the cohesin ring structure (Cuadrado and Losada, 2020; Nasmyth and Haering, 2009; Piché et al., 2019; Remeseiro et al., 2013). Cohesin dependency has been demonstrated by depletion of various cohesin units (Piché et al., 2019). Cohesin release from chromatin is driven by WAPL, which opens an exit site at the interface of the SMC3/SCC1 subunits of the cohesin ring (Haarhuis et al., 2013, 2017; Silva et al., 2020). Prior studies have elegantly demonstrated that the absence of WAPL reduces cohesin turnover, alters chromatin loop extensions, and leads to defects in interphase chromosome organization (Busslinger et al., 2017; Haarhuis et al., 2013, 2017; Hill et al., 2020; Silva et al., 2020; Tedeschi et al., 2013).

WAPL is essential during mammalian embryonic development (Tedeschi et al., 2013). However, the role of WAPL-dependent chromatin alterations on *in vivo* functions after embryonal development or in mature T cells is not known. The 3D chromatin landscape has been recently described in T cell development, in T cell lines, and following *in vitro* stimulation (Hu et al., 2018; Isoda et al., 2017; Misteli, 2020; Rawlings et al., 2011; Robson et al., 2017; Yang et al., 2020; Burren et al., 2017; Bediaga et al., 2021). It remains unclear, however, whether the specific changes in the 3D chromatin landscape influence or emerge from T cell development. Furthermore, the functional chromatin landscape in mature T cells and their alterations following *in vivo* activation remain unknown. The role of cohesin ring formation in mature T cell

¹Department of Internal Medicine, Division of Hematology and Oncology, University of Michigan Rogel Cancer Center, Ann Arbor, MI, USA

²Department of Computational Medicine and Bioinformatics, University of Michigan, Ann Arbor, MI 48109, USA

³Department of Mathematics, University of Michigan, Ann Arbor, MI, USA

⁴These authors contributed equally

⁵Lead contact

*Correspondence: reddypr@med.umich.edu
<https://doi.org/10.1016/j.isci.2022.104846>



development, its function *in vivo*, and its disruption by the absence of WAPL in mature T cell immunity are also not fully understood.

Mature T cells can cause graft-versus-host disease (GVHD) following allogeneic hematopoietic cell transplantation (HCT), a potentially curative therapy against many hematological malignant and nonmalignant diseases (Blazar et al., 2020; Wu and Reddy, 2017; Zeiser and Blazar, 2017). GVHD has precluded widespread utilization of this effective therapy. The chromatin landscape of allogeneic T cells and whether the disruption of this landscape can regulate the severity of T-cell-mediated GVHD remains unexplored.

Herein, we utilized genome-wide chromosome conformation capture (Hi-C) and RNA sequencing to describe the 3D chromatin architecture of mature T cells *in vivo*, specifically at baseline (unstimulated, naive, pretransplant) and following nonantigen-stimulated lymphopenia-induced proliferation (syngeneic) and alloantigen-driven (allogeneic) stimulation (Maeda et al., 2007) (Figure S1). We evaluated 3D chromatin architecture at the chromosome, TAD, and sub-TAD levels to capture both global and local trends of T cell genome structure. We generated T-cell-specific WAPL-deficient mice and demonstrated that WAPL regulates the 3D chromatin structure, function, and *in vivo* biological response of T cells such as GVHD. These data collectively demonstrate that a *priori* disruption of chromatin structure regulates mature T cell function.

RESULTS

Characterization of mature naïve T cell genome architecture following *in vivo* stimulation

We first determined the genome architecture of mature naïve T cells at baseline and following *in vivo* lymphopenic and antigen-driven stimulation. To mimic clinically relevant *in vivo* stimulation, we compared naïve T cells before and after experimental syngeneic and allogeneic transplantation. To this end, we utilized MHC-disparate B6 into a BALB/c model of transplantation (Reddy et al., 2008). CD62L⁺ naive donor T cells were harvested from the splenocytes of B6 donors and transplanted into congenic syngeneic B6 or allogeneic BALB/c recipients (see STAR Methods). Recipient animals were sacrificed 7 days after transplantation, and their splenic T cells were isolated using congenic markers and analyzed for genomic architecture. Although we generated Hi-C contact maps to profile genome-wide chromatin interactions (Rao et al., 2014) for harvested T cells, variability in the number of mappable Hi-C reads among unstimulated and stimulated T cell settings (Table S1) precluded us from reliably making direct comparisons between the genome architecture of naive, syngeneic, and allogeneic T cells. From the RNA-seq data, however, we did observe significant differences in gene expression ($|\log_2FC| \geq 1$, $p \leq 0.001$) before and after *in vivo* stimulation (Figure S2).

Generation of T cell conditional WAPL-deficient mice

Because T cell function changed following stimulation, we next sought to evaluate which conformational features in the genome are critical for T cell function. Cohesin promotes chromatin looping, whereas WAPL is important for the release of cohesin from chromatin. WAPL is essential for embryonal development, and its deficiency has been shown to cause defects in chromatin structure (Tedeschi et al., 2013). Specifically, WAPL has been shown to restrict chromosome loop extension (Busslinger et al., 2017; Haarhuis et al., 2017; Haarhuis and Rowland, 2017; Hill et al., 2020). In addition, we previously demonstrated that mir142 regulates mature T cell proliferation, targets WAPL expression in T cells, and that it may modulate T cell activation (Sun et al., 2013). Therefore, we determined whether WAPL regulates 3D chromatin architecture and the function of mature T cells.

Because WAPL is critical for embryonal development, we generated a T cell conditional *Wapl* knockout (KO) mouse using CRISPR-Cas9 and CD4-CRE systems (Ran et al., 2015; Tabebordbar et al., 2016). The *Wapl* locus on chromosome 14q has 18 exons and one noncoding exon (Figure S3A). We designed two sgRNAs specific to exon 2 of the *Wapl* gene to generate a double strand break in exon 2 (Figures 1A and S3B). Our first line of mice carried an insert of two sgRNAs targeting exon 2 in *Wapl* (Figures 1A and S3C). The second and third lines carried Rosa26-floxed STOP-Cas9 knock-in on B6J (The Jackson Laboratory, Stock No:026175) or were CD4-CRE transgenic mice (The Jackson Laboratory, Stock No: 017336) (Figure S3C). Triple crosses were screened for sgRNA insert showing the positive 457 bp band (sgRNA-Wapl) (Figure 1B), CRE positive as a 100 bp band, loxP-SV40pA x3-loxP-CAS9-GFP (LSL) cleavage activity demonstrating 1,123 bp for WT LSL, and a 285 bp band for cleaved LSL after CRE recombination processing. The conditional KO mice developed normally. The *Wapl* KO T cells were verified for GFP

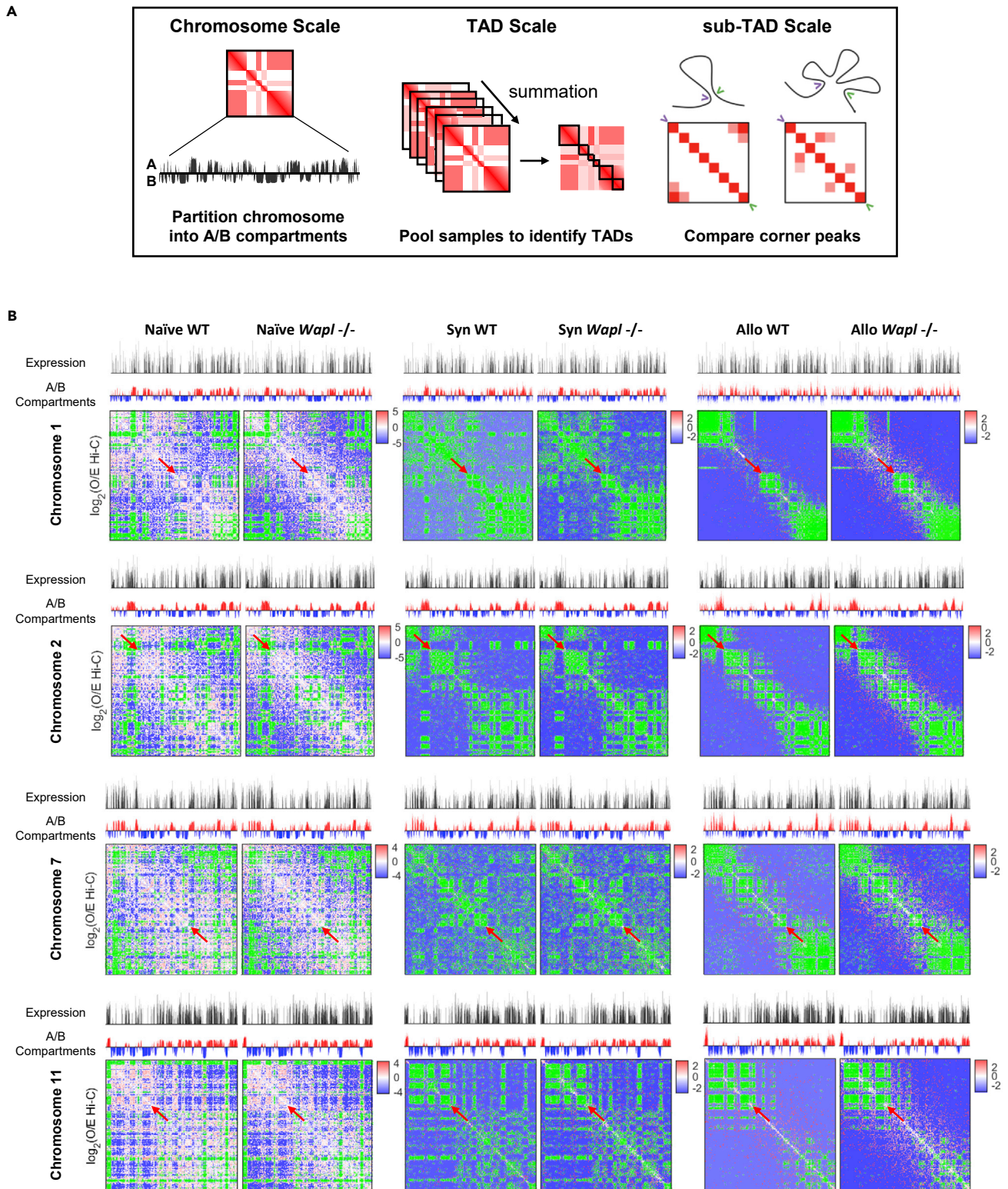


Figure 2. Genome-wide effects of WAPL knockout in unstimulated naïve T cells and after syngeneic/allogeneic transplantation

(A) Illustration of hierarchical Hi-C analysis workflow.

(B) Chromosome-level features and contact maps for chromosomes 1 and 2 from WT and *Wapl* knockout T cells. Gene expression (top track) is shown as a vector of $\log_2(\text{TPM})$ values binned at 100 kb resolution, and chromatin accessibility (bottom track) is shown as signed values from the Fiedler vector of the

Figure 2. Continued

Hi-C contact map where positive values (red) denote A compartments and negative values (blue) denote B compartments. ICE and O/E normalized Hi-C contact maps are shown at 100-kb resolution and log-scale. Matrix dissimilarity between WT and KO conditions was detected by the Larntz-Perlman procedure (see [STAR Methods](#)) and genomic regions with dissimilarity in the 99th percentile are shaded in green. These areas indicate the largest perturbations to the chromatin architecture upon *Wapl* knockout.

expression ([Figure 1B](#)). The higher levels of LSL cleavage and GFP expression assured successful depletion of WAPL ([Figure 1B](#), lane 4). We further confirmed WAPL protein depletion through western blotting ([Figure 1C](#)) in T cells isolated from multiple knockout pups. Finally, to further confirm efficient deletion, we performed RNA-seq on the T cells sorted from these mice and compared them with littermate WT T cells, which demonstrated efficient loss of exon 2 in the *Wapl* gene ([Figure 1D](#)).

WAPL regulates T cell genome architecture

Because WAPL is known to regulate genome architecture and genome architecture entrains transcription ([Kueng et al., 2006](#); [Tedeschi et al., 2013](#); [Wutz et al., 2017](#)), we next evaluated the impact of WAPL deficiency on genome architecture and gene expression of unstimulated naïve T cells. To analyze whole-genome architecture (structure) and gene expression (function), we integrated Hi-C and RNA-seq data (see [STAR Methods](#)). We studied changes in genome structure and function at the chromosome, TAD, and sub-TAD levels ([Figure 2A](#)). RNA-seq was performed on T cells harvested from naïve B6 and those harvested on day+7 from transplanted syngeneic and allogeneic B6 recipients (see [STAR Methods](#)).

We evaluated the statistical dissimilarity between wild-type (WT) and knockout (KO) Hi-C contact matrices at the chromosome level in each setting by employing the Larntz-Perlman (LP) procedure (see [STAR Methods](#)), which revealed regions critically impacted by *Wapl* knockout. WT and KO matrices were significantly dissimilar across all chromosomes ($p < 0.001$). Although statistically different, WT and KO chromosomes in unstimulated naïve T cells, except for chromosomes 16 and 19, had a lesser number of differential regions when compared with WT and KO chromosomes in syngeneic or allogeneic T cells ([Figure 2B](#) and [Table S2](#)). This conservation of structure is consistent with the notion that unstimulated naïve T cells are in a quiescent-like state and therefore less impacted by the loss of WAPL.

We highlight regions in the 99th percentile of significant changes across chromosomes 1, 2, 7, and 11 in [Figure 2B](#), due to their abundance of differential expression and compartmentalization ([Figures S4](#) and [S5](#)). Across all naïve chromosomes, 15%–25% of genes within these LP-dissimilar regions are significantly differentially expressed ($p < 0.05$) compared with 8.5%–13% across LP-dissimilar regions of syngeneic chromosomes and 3%–7% across LP-dissimilar regions of allogeneic chromosomes. Interestingly, there are differential regions in common between the syngeneic and allogeneic settings that are not detected in the naïve setting (red arrows in [Figure 2B](#)), indicating stimulation-specific genome architecture.

We then bi-partitioned chromosomes into individual stretches of accessible (active) and inaccessible (inactive) chromatin, termed A (euchromatin) and B (heterochromatin) compartments, respectively ([Lieberman-Aiden et al., 2009](#)). We demarcated these regions using the signed values of the Fiedler vector that measures underlying chromatin accessibility ([Chen et al., 2015](#)). The positive values of the Fiedler vector reflect compartment A and negative values reflect compartment B. We observed A/B compartment switch events mediated by the loss of WAPL in all settings ([Figure S5](#)). Across all chromosomes, 184 genomic bins (100kb-length) containing 217 genes in the unstimulated naïve KO T cells occupied a different compartment when compared with WT T cells ([Figure S5](#)). These switch events demonstrated a bias from compartment B to compartment A (70.7% of switch events) ([Figure S5](#)).

In the context of lymphopenic stimulation (syngeneic), KO T cells exhibited 303 switch events involving 375 genes when compared with WT T cells. In the allogeneic context, KO T cells demonstrated 413 switch events involving 485 genes when compared with WT T cells ([Figure S5](#)). The switch bias was once again in the direction of compartment B to compartment A in syngeneic T cells (60.4% of switch events) and in allogeneic T cells (53.8% of switch events). In addition, allogeneic T cells had more switch events per chromosome than unstimulated naïve and syngeneic T cells ([Figure S5](#)). Interestingly, switched compartment loci tended to congregate toward the ends of chromosomes rather than in the middle or spread evenly throughout. No switch events were observed among contiguous regions of the genome in any of these settings. Overall, 14%, 68%, and 70% of switch events in naïve, syngeneic, and allogeneic T cells, respectively, occurred within the previously identified LP-dissimilar regions. Although there are coordinated changes in

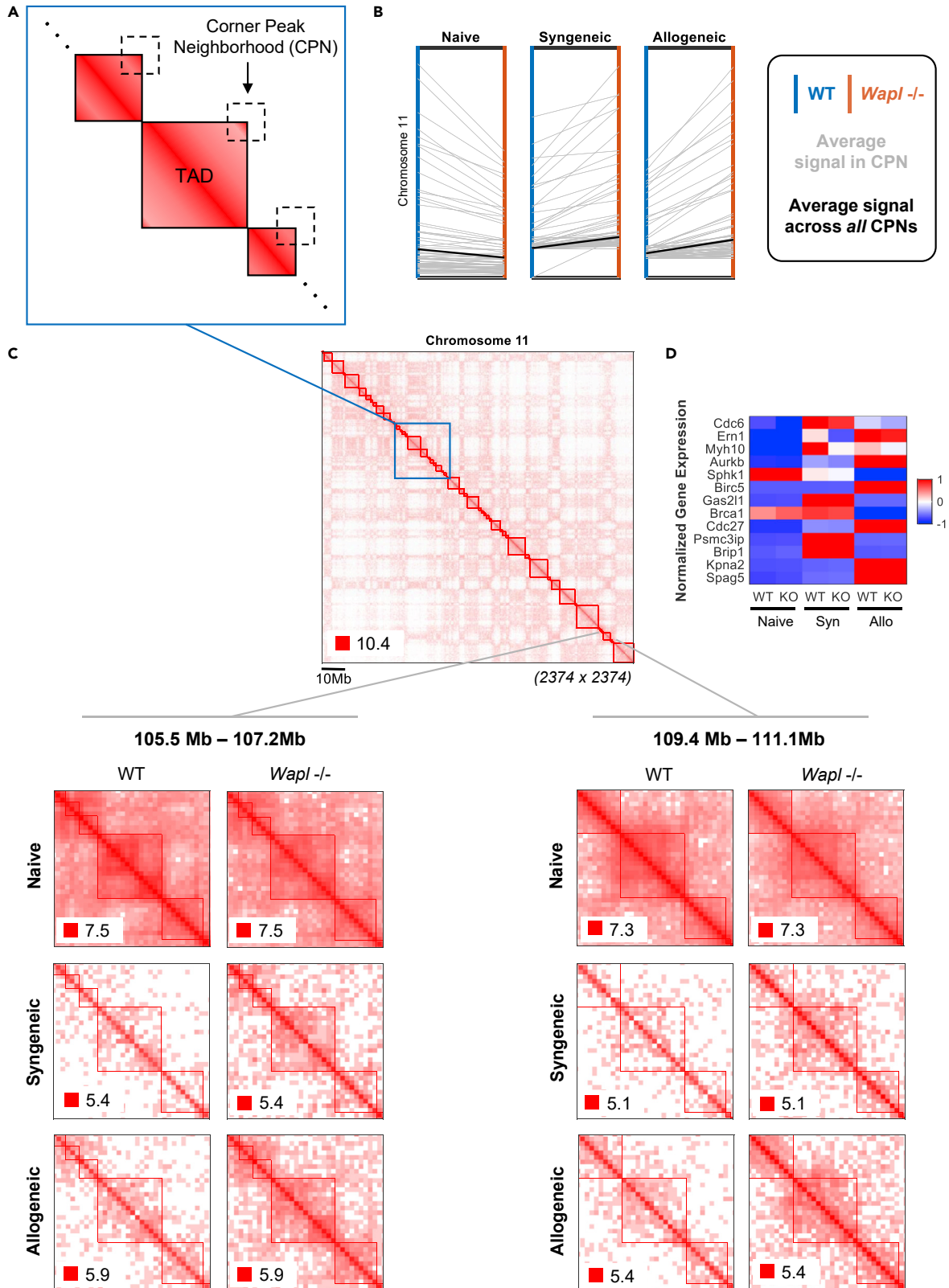


Figure 3. Comparison of internal TAD organization between WT and KO T cells

(A) Schematic of TADs illustrating how “corner peaks”—interactions between opposite TAD boundaries—were characterized in terms of their local neighborhoods. The nonzero mean of absolute read counts in each local corner peak neighborhood (CPN) was used to define the strength of TAD boundary interactions.

(B) Change in corner peak signal from WT (blue axis) to KO (orange axis) for each TAD (individual gray lines) on Chromosome 11. The average change in corner peak signal between the two conditions is plotted as a solid black line in each panel to capture the overall trend across settings. TADs and their corner peak signals are represented at 50 kb resolution.

(C) (Top center) Chromosome 11 observed contact map pooled across samples at 50 kb resolution. (Bottom left) TAD region of Chromosome 11 extending from 105.5 Mb to 107.2 Mb capturing corner peak increase from WT to KO most notably in the syngeneic and allogeneic settings; differential expression of gene *Wipi1* occurs in the centermost TAD in this region. (Bottom right) TAD region of Chromosome 11 extending from 109.4 Mb to 111.1 Mb capturing corner peak increase from WT to KO; differential expression of gene *Cdc42ep4* occurs in the centermost TAD in this region.

(D) Heatmap of differentially expressed cell-cycle genes residing on Chromosome 11.

expression and chromatin accessibility genome-wide and most notably at LP-dissimilar regions, chromatin compartmentalization largely remained stable between WT and KO T cells (Table S3).

WAPL impacts internal structure of TADs and local gene transcription

Stability in global compartment organization throughout the genome does not preclude changes to local genome organization. Chromatin preferentially interacts within locally distributed and insulated regions called topologically associating domains (TADs) that regulate transcription (Dixon et al., 2012). Thus, we next analyzed the impact of WAPL depletion in TADs. One highly supported mechanism of TAD formation is loop extrusion (Fudenberg et al., 2016) mediated by the ring-shaped cohesin complex and WAPL, which enables TAD dynamics by promoting cohesin turnover (Haarhuis et al., 2017). Specifically, genes residing in the same TAD experience coordinated regulation and expression (Dixon et al., 2012; Nora et al., 2012; Shen et al., 2012; Le Dily et al., 2014), whereas changes to TAD boundaries due to altered CTCF binding influence anomalous gene-enhancer interactions (Flavahan et al., 2016; Lupiáñez et al., 2015).

We therefore utilized spectral graph theory to identify the positional boundaries that define TADs (Chen et al., 2016). TADs have been widely suggested to be highly conserved across cell types and conditions in mammalian genomes (Dixon et al., 2012; Nora et al., 2012; Rao et al., 2014), so we pooled our Hi-C data across settings to enable higher resolution binning of the data and reliable detection of TAD boundaries within chromosomes (see STAR Methods).

TAD analysis revealed the emergence of a unique feature in the context of syngeneic and allogeneic T cells in the absence of WAPL—the appearance of “corner peaks.” Corner peaks are the enrichment of interaction frequency at domain boundaries seen at the bottom left and top right corners of TADs (Rao et al., 2014). To evaluate differences in corner peak signal between WT and KO T cells, we established a local neighborhood around the corners of each TAD and determined the average number of observed contacts in each neighborhood (Figure 3A). On aggregate, we observed that corner peaks became more pronounced upon WAPL depletion in syngeneic and allogeneic T cells (Figures 3B and S6), consistent with the known activity of WAPL to limit loop extension (Haarhuis and Rowland, 2017; Haarhuis et al., 2017). Further, several studies have demonstrated that corner peaks are associated with a longer residence time of the cohesin complex at TAD borders (Haarhuis et al., 2017; Schwarzer et al., 2017; Szabo et al., 2019). We did not, however, observe this rise in corner peak abundance in the KO unstimulated naïve T cells, but rather a decrease (Figures 3B and S6), suggesting that the development of corner peaks in stimulated T cells might be a consequence of their proliferation following activation.

When compared against a background set of interactions—surrounding interactions occurring at a comparable distance to opposing TAD boundaries—we found that the rise in corner peak signal from WT to KO in syngeneic and allogeneic T cells was statistically significant in a large proportion of TADs ($p < 0.01$, Table S4). We next determined whether there was any functional significance to the observed corner peak dynamics. Syngeneic T cells harbored the most significantly differentially expressed genes (DEGs) ($|\log_2FC| \geq 1$, $p \leq 0.01$) between WT and KO out of all settings (297 in naïve, 566 in syngeneic, and 46 in allogeneic) and had a particularly high concentration of DEGs on chromosome 11 (58 DEGs, Figure S4). Given this functional dissimilarity, we further investigated intra-TAD interactions on Chromosome 11 at 50 kb resolution (Figure 3C) and present an earlier iteration of this analysis on Chromosome 7 at a lower 100 kb resolution in Figure S6.

We were particularly interested in identifying regions where differential expression overlapped with increases in corner peak signal. We noted statistically significant corner peak increases in 3 naïve, 47 syngeneic, and 50 allogeneic TADs upon WAPL deletion across Chromosome 11, respectively. Of the TADs exhibiting these corner peak increases, 2 contained DEGs in naïve T cells, 10 in syngeneic T cells, and 3 in allogeneic T cells. We highlighted two such regions on Chromosome 11 (Figure 3C, bottom left and right). The first region we observed ranged from position 105.5Mb to 107.2 Mb on Chromosome 11 and encompassed a TAD exhibiting a significant corner peak signal increase most notably in the syngeneic and allogeneic contexts. Furthermore, this TAD contains the gene, *Wipi1*, which exhibited a 2.8-fold increase in expression from WT to KO in syngeneic cells yet a less significant 0.8-fold increase in expression from WT to KO in both naïve and allogeneic T cells. Another stand-out TAD within region 109.4Mb–111.1Mb on Chromosome 11 demonstrated differential expression of *Cdc42ep4* in syngeneic T cells with a 1.5-fold increase in expression upon WAPL deletion. Overall, Chromosome 11 contained 25 DEGs in naïve T cells, 58 DEGs in syngeneic T cells, and 4 DEGs in allogeneic T cells dispersed across several TADs.

Impact of WAPL on the cell-cycle gene network

WAPL is critical for sister chromatid cohesion and loop extrusion dynamics. These processes correlate with cellular proliferation and cell cycling, and because we observed notable changes in corner peaks of Chromosomes 7 and 11 only in the context of syngeneic and allogeneic settings in the absence of WAPL, we next explored changes in cell-cycle genes and the TADs that these genes reside in. One gene-rich region in Chromosome 7, extending between positions 60Mb and 70Mb on the chromosome, exhibited considerable intra-TAD reorganization in the KO T cells when compared with WT unstimulated (Figure S7D), syngeneic (Figure S7E), and allogeneic (Figure S7F) T cells. This region contains cell-cycle genes (Dolatabadi et al., 2017; Inaba et al., 2018): *Fanci*, *Prc1*, and *Blm*. These cell-cycle genes (*Fanci*, *Prc1*, and *Blm*) were not significantly differentially expressed, as they did not meet the cutoff of $|\log_2FC| \geq 1$. However, there were seven non-cell-cycling genes (*Mesp2*, *Arpin*, *Fes*, *Homer2*, *Saxo2*, *Cemip*, and *Arnt2*) directly upstream and downstream of the cell-cycle genes in this region that were significantly differentially expressed. These data suggest that in the unstimulated KO T cells, these three cell-cycle genes on Chromosome 7 were not differentially expressed despite the changes in intra-TAD interactions when compared with WT T cells. Similar to the unstimulated context, in the syngeneic T cells, there was a differential expression of non-cell-cycle genes upstream and downstream of cell-cycle genes in this region (*Agbl1*, *Isg20*, *Can*, *Hapln3*, *Ribp1*, *Mesp2*, *Anpep*, *Fes*, *Slc28a1*, *Homer2*, *Adamtsl3*, and *Tmc3*). In allogeneic T cells, non-cell-cycle genes (*Agbl1*, *Can*, *Rhcg*, and *Adamtsl3*) once again were differentially expressed. Thus, in the absence of WAPL, the highlighted region of Chromosome 7 containing the three cell-cycle genes did not dynamically change but demonstrated significant changes in the expression ($|\log_2FC| \geq 1$, $p \leq 0.05$) and internal structural rearrangement of genes in their vicinity. No other cell-cycle genes on Chromosome 7 demonstrated differential expression.

Chromosome 11 contained 13 differentially expressed cell-cycle genes (Figure 3D). Of these 13, only one gene (*Gas2l1*) was significantly differentially expressed between naïve WT and KO T cells, two genes (*Myh10* and *Sphk1*) between syngeneic WT and KO T cells, and none in the allogeneic setting. We did not however observe an overlap between the differential expression of these genes and TADs with altered internal TAD structure. Although WAPL depletion did not disrupt the cell cycling transcriptional program within unstimulated and stimulated contexts much on Chromosome 11, the expression of these genes was quite different between contexts (Figure 3D).

Although we did not see a change in the three cell-cycle genes noted earlier in the analysis of Chromosome 7 nor significant coupling of cell-cycle differential expression and corner peak dynamics on Chromosome 11, WAPL is known to regulate cell cycling so we next explored the entire breadth of cell-cycle genes throughout the genome. To this end, we extracted and stitched together 141 Hi-C genomic bins that corresponded to a curated set of 170 cell-cycle genes genome-wide, generating a Hi-C-derived 5C contact matrix (see STAR Methods). 5C, like Hi-C, is a derivative of the original chromosome conformation capture technique (Dekker et al., 2002) and is useful in identifying interactions among select genomic regions that bear relationship to one another (Dostie et al., 2006). In unstimulated naïve T cells, we observed that the connectivity of the cell-cycle network decreased in the absence of WAPL, as determined by the element-wise Pearson correlations moving toward zero (Figure 4A). In syngeneic and allogeneic T cells,

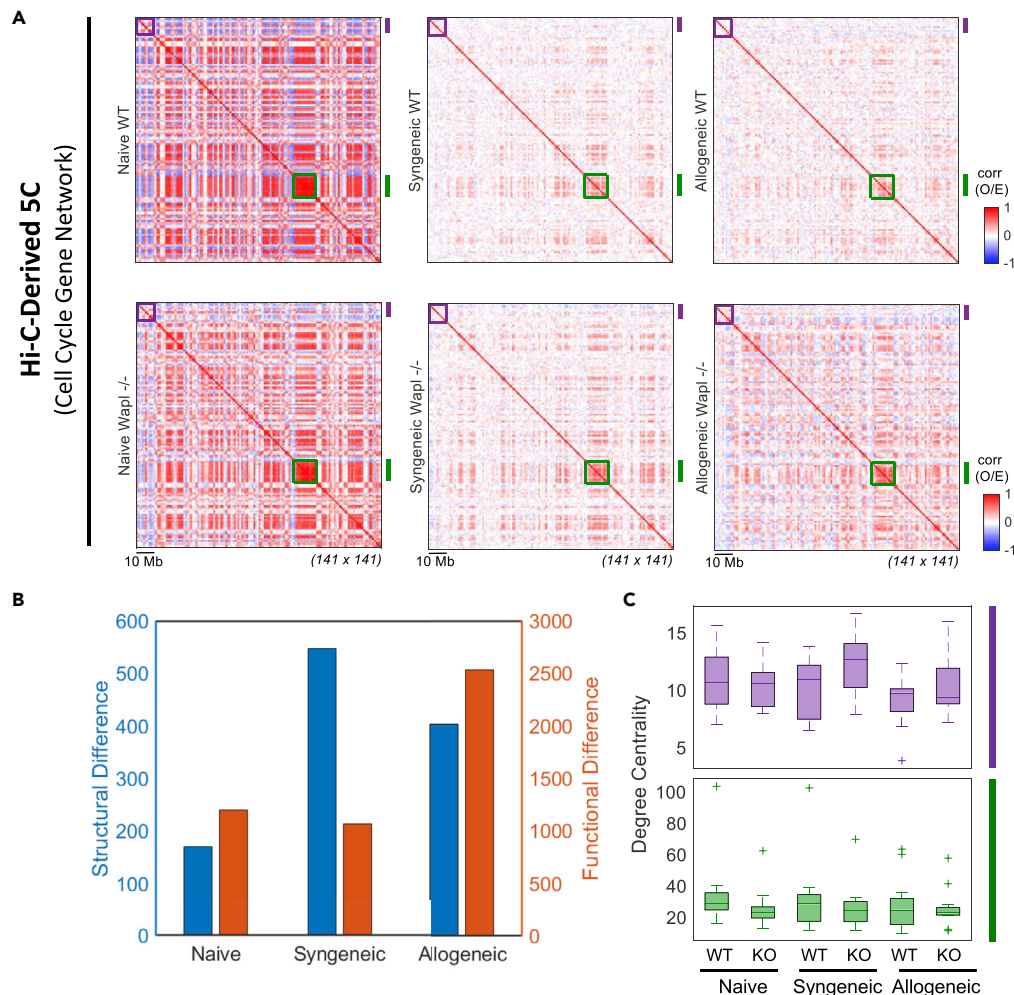


Figure 4. Cell-cycle gene network across T cells

(A) Hi-C-derived 5C contact maps representing the cell-cycle gene network. Rows and columns correspond to genomic bins across all chromosomes that contain cell-cycle genes. Maps are shown at 1-Mb resolution as a Pearson correlation of normalized (observed/expected) contacts. The purple and green boxes highlight subgroups of interest that are assessed in C. The purple subgroup is comprised of 10 loci (1Mb length) ranging noncontiguously from 18 Mb to 197 Mb and containing 10 cell-cycle genes. The cell-cycle gene loci in WT and KO T cells in each subgroup is comprised of 12 loci (1Mb length) ranging noncontiguously from 1,489 Mb to 1,606 Mb and containing 16 cell-cycle genes.

(B) Structural and functional differences between all cell-cycle gene loci in WT and KO T cells in each setting. Difference is measured as the Frobenius norm of the difference between WT and KO data (see STAR Methods). The left y axis (blue) reflects the Frobenius norm of the difference between WT and KO Hi-C matrices (measure of structural change) in each setting and the right y axis (orange) reflects the Frobenius norm of the difference between WT and KO gene expression vectors (measure of functional change) in each setting.

(C) Degree centrality (i.e. the row sum of a matrix) of subgroups of interest.

however, connectivity appeared to strengthen in the absence of WAPL, as demonstrated by the correlation tending towards ± 1 (Figure 4A).

The connectivity (structure) of cell-cycle genes changed between the WT and KO T cells in all settings, but the maximal change was noted in the syngeneic setting (Figure 4B). However, changes in the structure of the cell-cycle network did not trend with the function (expression). The expression (function) of the cell-cycle gene network changed the most between WT and KO T cells in the context of allogeneic setting (Figure 4B). The genome-wide structural analysis of the cell-cycle gene network highlighted two subgroups of highly connected genes (shown in purple and green boxes in Figure 4A). One of these subgroups negatively correlated with most of the network (Figure 4A, purple box), whereas the other demonstrated

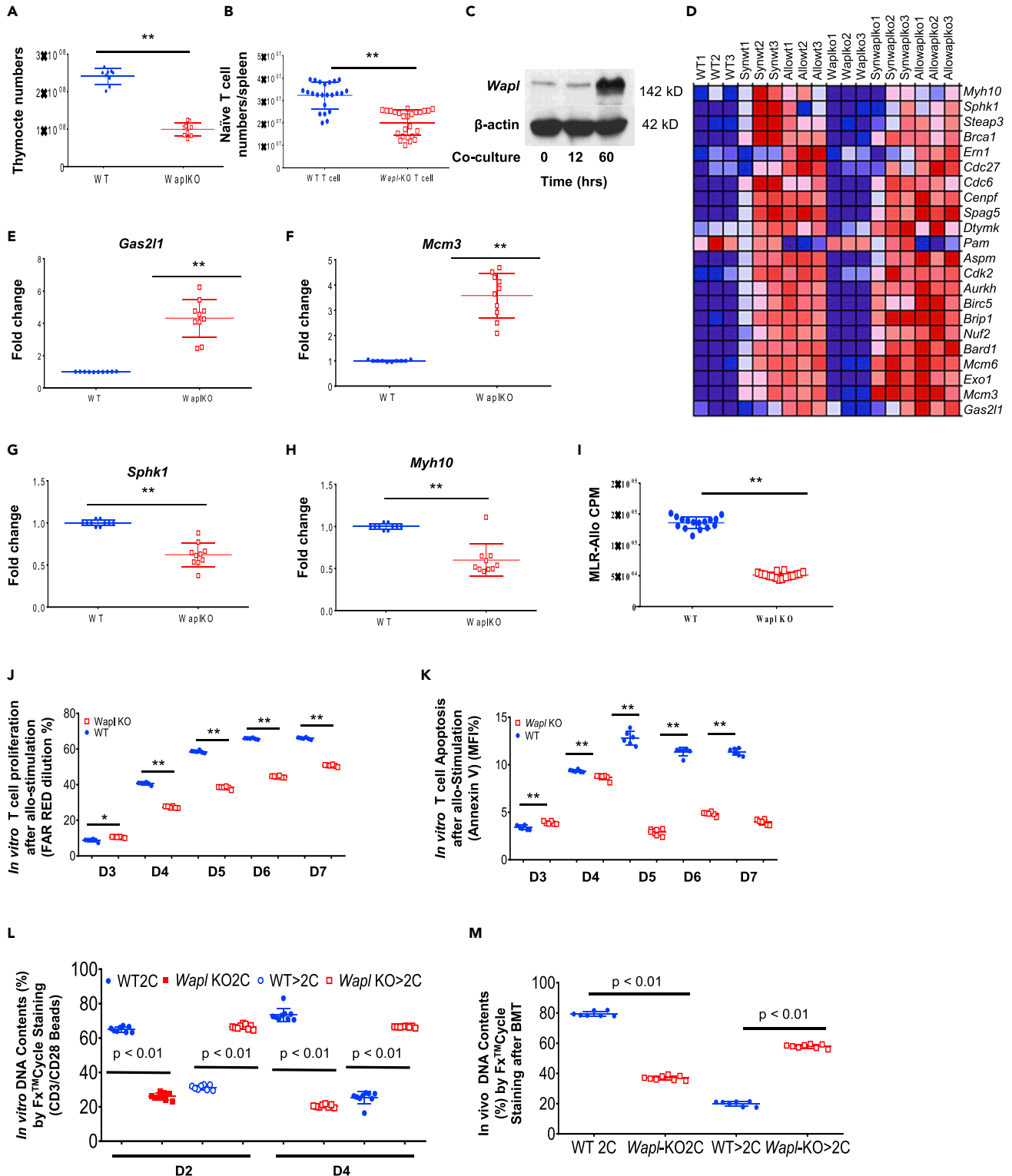


Figure 5. WAPL deficiency impairs T cell development, proliferation, and cell cycling

(A) Total numbers of thymocytes isolated from WT and *Wapl* KO thymii were counted. Data were combined from WT (9) and *Wapl* KO (10) mice (mean \pm SEM).

(B) Total T cell numbers of spleens from WT and *Wapl* KO mice were counted. Data were combined from WT (23) and *Wapl* KO (26) mice (mean \pm SEM).

Figure 5. Continued

- (C) WAPL protein expression was upregulated in T cells when co cultured with allogeneic DCs *in vitro*. A representative western blot was shown.
- (D) mRNA expression of cell-cycle genes was analyzed through GSEA. Gene sets of WT and *Wapl* KO T cells from naïve, syngeneic, and allogeneic conditions were sorted by enrichment scores (ESs). All groups were in biological triplicates.
- (E–H) According to ESs in (D), the mRNA expressions of the top or bottom two scored genes were analyzed by quantitative real-time PCR. Data were combined from three independent experiments (mean \pm SEM).
- (I) H3-TdR incorporation in WT and *Wapl* KO T cells were analyzed by mixed lymphocyte reaction when stimulated by allogeneic DCs for 4 days. Data were combined from three independent experiments (mean \pm SEM).
- (J) Cell proliferation was analyzed by Far-Red dilution for either WT or *Wapl* KO T cells when stimulated with allogeneic DCs for up to 7 days. Data were combined from two independent experiments (mean \pm SEM).
- (K) Cell apoptosis was analyzed by FACS after An-nexin V staining for WT and *Wapl* KO T cells when stimulated with allogeneic DCs for up to 7 days. Data were combined from two independent experiments (mean \pm SEM).
- (L) After WT and *Wapl* KO T cells were stimulated with CD3/CD28Ab for 2–4 days *in vitro*, cells were stained with FxCycle™Far-Red, DNA contents were separated as 2C and >2C by flow cytometry. Combined data were obtained from three independent experiments (mean \pm SEM).
- (M) WT and *Wapl* KO T cells were isolated from recipient spleens on day 7 after allogeneic BMT *in vivo* and were stained with FxCycle™Far-Red; DNA contents were separated as 2C and >2C by flow cytometry. Combined data were obtained from two independent experiments (mean \pm SEM).

positive correlation with most of the network (Figure 4A, green box) in all three settings. The measure of interconnectivity within these two subgroups, in terms of degree centrality, is shown in Figure 4C. Ultimately, although gene expression of cell-cycle genes *Fanci*, *Prc1*, and *Blm* did not change in the absence of WAPL, other genes in the cell-cycle network did change significantly (Table S5). Five cell-cycle genes were upregulated in the absence of WAPL in unstimulated naïve T cells. By contrast, 12 cell-cycle genes were downregulated and 4 upregulated between WT and KO T cells in the syngeneic context. In the context of alloantigen stimulation, only one gene was downregulated.

WAPL-induced changes in genome structure alter T cell gene expression

We next determined whether the changes in the chromatin architecture related to WAPL deficiency in T cells affected genome function. Three-dimensional genome structural changes have been suggested to affect T cell development (Seitan et al., 2011). Whether *a priori* disruption of the cohesin ring affected T cell function, however, is not clear. The transgenic mice with conditional *Wapl* KO in T cells displayed normal birth and growth rates and generated enough mature naïve T cells. To better analyze the developmental impact of WAPL deficiency on T cell development, we next analyzed the thymii from 8- to 10-week-old WT and *Wapl* KO littermates. The thymocytes from the *Wapl* KO animals showed significant changes when compared with the WT littermate controls. Specifically, they showed reduction in the total number of thymocytes, double positive (DP), and CD8 SP thymocytes (Figures 5A and S8A).

We next analyzed the secondary lymphoid organ (spleens) for peripheral T cell subsets. *Wapl* KO littermates demonstrated lower numbers of total T cells in the spleen (Figure 5B) and lower numbers of CD3⁺CD4⁺ and CD3⁺CD8⁺ T cells (Figures S8B and S8C) when compared with WT littermates. During the β -selection checkpoint in the thymus, the β chain of the T cell receptor rearranged by the thymocytes must retain the structural properties allowing it to be presented on the surface of the thymocytes. We therefore screened for TCR β ⁺ CD4⁺ and CD8⁺ T cells in the spleen and found that the *Wapl* KO mice demonstrated lower numbers of TCR β ⁺ CD4⁺ and CD8⁺ T cells in the spleen when compared with WT littermates (Figures S8D and S8E). The splenocytes from the KO animals also demonstrated lower numbers of CD3⁺CD69⁺, CD4⁺CD69⁺, CD8⁺CD69⁺, and CD4⁺CD25⁺ T cells (Figures S8A–S8D).

Because WAPL deficiency altered chromatin architecture, we next analyzed whether these structural changes were associated with changes in gene expression and proliferation, at baseline and following *in vivo* stimulation. To this end, we first determined whether *Wapl* expression itself changed in T cells following stimulation. Consistent with our previous observation, we observed significant upregulation of WAPL protein in T cells upon co-culture with allogeneic DCs for 60 h (Figure 5C) (Sun et al., 2015, 2019). To determine the impact of this structure-function relationship, we performed gene set enrichment analysis (GSEA) for the cell-cycle gene network highlighted in our earlier Hi-C-derived 5C analyses (Figure 4). We found that cell-cycle genes were differentially regulated between WT and WAPL-deficient T cells (Figure 5D). We verified results with real-time quantitative PCR. *Gas2l1*, a gene induced upon growth arrest (Goriounov et al., 2003), and *Mcm3*, which increases as cells progress from G0 into the G1/S phase and regulates the cell cycle (Tsuruga et al., 1997), were significantly upregulated in WAPL-deficient T cells compared with WT T cells (Figures 5E and 5F). In contrast, *Sphk1*, a gene that plays a key role in TNF- α signaling and the canonical NF- κ B activation pathway important in inflammatory, apoptotic, and immune

processes (Alvarez et al., 2010), and *Myh10*, a gene required for completion of cell division during cytokinesis (Kim et al., 2005; Straight et al., 2003), were both downregulated in WAPL-deficient T cells (Figures 5G and 5H). These observations demonstrated that changes in genome structure related to WAPL deficiency in T cells promote differential gene expression that suppresses apoptosis, cell proliferation, and cell-cycle progress.

To further investigate the impact of WAPL deficiency on T cell cellular responses, we stimulated WAPL-deficient and WT T cells *in vitro*, either with alloantigen stimulation in mixed lymphocytes reaction (MLR) by co-culturing T cells with allogeneic DCs for 4 days or with CD3/CD28Ab for 2 or 3 days and pulsed with H3-TdR. The WT T cells demonstrated significantly greater H3-TdR incorporation when compared with *Wapl* KO T cells, suggesting that WAPL deficiency caused reduced proliferation (Figures 5I and S9E). T cell proliferation was directly assessed *in vitro* using a dye dilution assay. Specifically, we utilized Cell Trace™FarRed dilution to avoid the interference with GFP fluorescence in *Wapl* KO T cells. The *Wapl* KO T cells demonstrated reduced dye dilutions when compared with WT T cells upon stimulation by either allogeneic DCs or CD3/CD28ab (Figures 5J and S8F). It is possible that cell death from apoptosis could contribute to the reduction in T cell expansion related to WAPL deficiency. We therefore also determined apoptosis after stimulation of both WT and *Wapl* KO T cells. The WAPL-deficient T cells also showed significantly decreased apoptosis when compared with littermate WT T cells (Figure 5K). These data demonstrate that the absence of WAPL altered T cell proliferation and apoptosis following *in vitro* stimulation.

The interaction between cohesin and WAPL plays an essential role in maintaining chromosome structure and separation of sister chromatids during mitosis and cell proliferation (Peters and Nishiyama, 2012). With the coordinated changes in expression of cell-cycling genes and genomic architecture in the absence of WAPL, and the reduction in proliferation, we next examined cellular mechanisms underlying the reduced proliferative capacity of WAPL-deficient T cells following *in vitro* and *in vivo* stimulation. Specifically, we explored the hypothesis that altered gene expression of cell-cycling genes from the change in genomic architecture related to WAPL deficiency leads to a reduction in cell cycling. To assess kinetic cell cycling we utilized flow cytometry analyses of DNA content with FxCycleFar Red Stain to avoid interference from the GFP fluorescence in *Wapl* KO T cells. Purified WT or *Wapl* KO T cells were stimulated with CD3/CD28 T cell activator dynabeads and analyzed for 2C and >2C populations. *Wapl* KO T cells demonstrated significantly lower 2C percentages but higher >2C percentages when compared with WT T cells at several time points after CD3/CD28 stimulation (Figures 5L and S10A). We next analyzed whether the effect on cell cycling was observed *in vivo*. To this end, we once again utilized the allogeneic bone marrow transplantation (BMT) model system, where the host splenocytes were harvested and analyzed for WT or *Wapl* KO donor T cells as above. As shown in Figures 5M and S9B, the *in vivo* stimulation of WT and *Wapl* KO T cells demonstrated similar differences as from *in vitro* stimulation. These data indicated that *Wapl* KO T cells had cell-cycle deficiency, which impairs T cell proliferation and alters T cell function *in vitro* and *in vivo*, consistent with cell-cycle gene analyses by Hi-C-derived 5C (Figure 5), GSEA, and qPCR analyses (Figures 5D–5H).

WAPL deficiency in T cells improves survival after allogeneic BMT

Mature T cells in the allogeneic donor T cells are the principal mediators of GVHD, a major cause of mortality after allogeneic BMT. Because WAPL regulated mature T cell response following *in vitro* and *in vivo* alloantigen stimulation, we next determined whether this has a clinical impact on GVHD severity following experimental allo-BMT. To this end, we once again utilized the MHC mismatched B6 (H2) → BALB/c (H2d) mouse model where the congenic B6 animals served as the syngeneic controls. BALB/c recipient mice were lethally irradiated (800 cGy total body irradiation, split dose) and transplanted with T-cell-depleted WT BM from B6 donors along with purified mature T cells from the spleen of either WT or *Wapl* KO B6 animals (Sun et al., 2015). The recipient animals were monitored for survival and GVHD severity as described in STAR Methods.

We first determined whether WAPL expression changed after allo-BMT. Consistent with the *in vitro* alloantigen stimulation shown in Figure 5C, WT cells demonstrated higher expression of WAPL protein in donor T cells harvested from recipient spleens 7 days after allogeneic BMT when compared with syngeneic controls (Figure 6A). Survival analysis demonstrated that all the syngeneic animals survived, but the allogeneic animals that received WT T cells died with signs of severe clinical GVHD (Figure 6B). In contrast, allogeneic

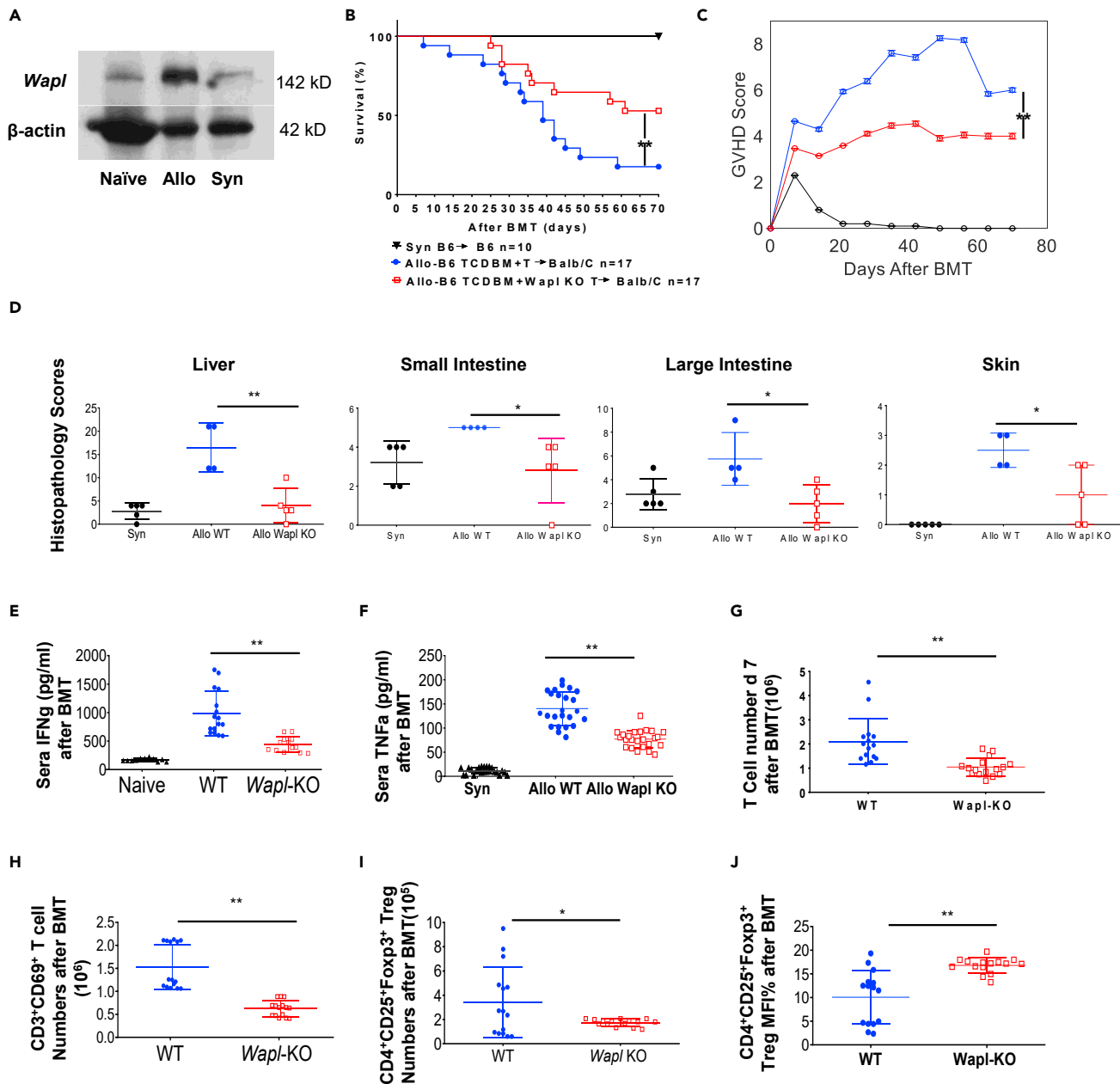


Figure 6. WAPL-deficient T cells mitigate GVHD severity in allogeneic BMT

(A) *Wapl* expression was upregulated in T cells on day 7 after allogeneic BMT. A representative western blot was shown.

(B) Allogeneic MHC mismatched B6 (H2b) into BALB/c(H2d) GVHD model. Survival percentages were recorded daily. p-values were obtained using the log rank test based on comparisons between animals that received either TCD BM plus WT T cells (blue circles) or TCD BM plus *Wapl* KO T cells (red squares). Combined data were from two independent experiments.

(C) GVHD score was assessed by a standard scoring system as before (Sun et al., 2015). The Mann Whitney U test was used for the statistical analysis of clinical scores between animals that received either TCD BM plus WT T cells (blue circles) or TCD BM plus *Wapl* KO T cells (red squares). Combined data were from two independent experiments.

(D) Histopathological analysis of the B6 into BALB/c BMT model. Bowel (small and large intestine), liver, and skin were obtained after BMT on day 21. GVHD scores were from two independent experiments (mean \pm SEM).

(E and F) Sera were collected from recipient mice on day 21 after allogeneic BMT as in (B); the concentrations of IFN- γ and TNF- α were measured by ELISA. Significant lower concentrations of IFN- γ and TNF- α were detected in the sera collected from mice transferred with *Wapl* KO T cells. Combined data were from two independent experiments (mean \pm SEM).

(G) *In vivo* T cell expansion was determined by isolating transferred WT and *Wapl* KO in BALB/c recipients on day 7 after allogeneic BMT. Data were combined from three independent experiments (mean \pm SEM).

Figure 6. Continued

(H) Transferred donor T cells (WT and *Wapl* KO) were isolated from recipient's spleens on day 7 after allogeneic BMT and stained for CD3⁺ and CD69⁺. The absolute numbers of activated *Wapl* KO T cells (CD3⁺CD69⁺) were significantly lower than WT T cells. Data were combined from three independent experiments (mean ± SEM).

(I and J) Donor T cells were isolated as in (H) on day 7 after allogeneic BMT and stained for CD4⁺ 25⁺ FoxP3⁺ for identifying T regulatory cells. The absolute numbers of *Wapl* KO Treg cells were significantly lower than WT Treg cells (I), although the percentages were the same between WT and *Wapl* KO T cells (J). Data were combined from three independent experiments (mean ± SEM). p-values were obtained using unpaired t test.

animals that received WAPL-deficient T cells showed significantly improved survival (53% versus 17%; $p < 0.01$) (Figure 6B) and reduced clinical severity of GVHD ($p < 0.01$) (Figure 6C). We confirmed the reduction in GVHD with detailed histopathological analyses of GVHD target organs including the liver, gastrointestinal (GI) tract, and skin. As shown in Figure 6D, allogeneic animals that received T cells from WAPL-deficient donors had significantly reduced histopathological GVHD in the liver ($p < 0.01$), GI tract (SI and LI) ($p < 0.05$), and skin ($p < 0.05$) on day +21 after BMT. Consistent with reduced mortality, the recipients of allogeneic *Wapl* KO T cells demonstrated reduced serum levels of proinflammatory cytokines such as interferon gamma (IFN- γ) and tumor necrosis factor alpha (TNF- α) when compared with WT T cell recipients (Figures 6E and 6F).

The allogeneic animals that received WT or KO T cells demonstrated >98% donor engraftment on day 21, ruling out mixed chimerism or engraftment as a cause for reduction in GVHD. Furthermore, consistent with above results, *Wapl* KO T cells showed significantly reduced expansion when compared with WT donor T cells (Figure 6G) in the recipient spleens harvested 7 days after BMT, suggesting that the reduction in GVHD was a consequence of reduced expansion of alloantigen-stimulated T cells. Consistent with this, the allogeneic *Wapl* KO T cells demonstrated fewer absolute numbers of CD3⁺CD69⁺ cells (Figure 6H) and regulatory T cells (despite a higher percent) when compared with WT T cells (Figures 6I and 6J).

DISCUSSION

The cohesin complex and its regulators, such as WAPL, are critical determinants of 3D genome architecture, which regulates replication, repair, and transcriptional processes (Cuadrado and Losada, 2020; Misteli, 2020; Nasmyth and Haering, 2009; Remeseiro et al., 2013). Given the paucity of data on the genomic organization of mature T cells and its impact on T cell function *in vivo*, we describe the genome architecture of mature T cells following *in vivo* lymphopenic and allogeneic stimulation.

Prior to the availability of Hi-C methods, structural features of the T cell genome following *in vitro* stimulation were explored in a seminal paper by Kim et al. (2004). Since then, other studies have built on it with the advent of Hi-C techniques following *in vitro* stimulation of T cells with anti-CD3/CD28 (Yang et al., 2020; Burren et al., 2017; Bediaga et al., 2021). We now expand on those studies by exploring the changes following *in vivo* homeostatic and antigen-driven stimulation. Previously, chromosome 6 in differentiating T cells was explored in its entirety, although global spatial characterization was limited to chromosome territories (Kim et al., 2004). Here, we profile the entire genome architecture of mature T cells following *in vivo* activation, including local structures such as TADs. We further connect those changes to genome-wide functional changes in gene expression and T cell responses. Hu et al. demonstrated a key role for transcription factor BCL11B in the development of T cells and associated genome structure changes (Hu et al., 2018) but did not characterize the relevance of structural integrity to mature T cell functions. Our data focus on the genomic landscape of mature T cells. We define a mechanistic role for genomic architecture in the regulation of gene expression, cellular function, and biological responses *in vivo* that impact clinically relevant disease states such as GVHD. We find that differences in 3D genome architecture are a consequence of the cellular state of activation and that its disruption, by altering the function of the cohesin complex, contributes to the regulation of mature T cell functions in response to allogeneic-stimulation.

We explored the mechanistic relevance of genome structure to function (gene expression) and to the cellular functions and biological impact of mature T cells by deleting WAPL, a key regulator of genome structure. WAPL deletion led to reduction of long-range interactions in the baseline unstimulated state of naïve T cells. However, following lymphopenic (syngeneic) and antigen (allogeneic) activation, there was a greater amplification of longer-range interactions following WAPL deletion. This is consistent with

previous reports on WAPL-deficient cell lines (Haarhuis et al., 2017; Liu et al., 2021) and with the notion of extruded DNA loops beyond CTCF barriers (Allahyar et al., 2018). These data suggest that WAPL alters genomic architecture, at baseline and after activation of T cells.

The *in vivo* role for WAPL-mediated regulation of chromatin structure is crucial for embryonal development (Tedeschi et al., 2013). We now extend these studies and demonstrate that WAPL also regulates *in vivo* immune responses mediated by T cells. T-cell-specific WAPL-deficient animals developed normally despite the T cells showing genomic structural changes at homeostasis. Upon stimulation, WAPL-deficient T cells demonstrated mitosis defects and more axial structures during interphase, suggesting that they exit mitosis with less intact cohesin. However, it is important to note that the absence of WAPL neither caused a complete loss of development of T cells nor a total shutdown of mature T cell proliferation. The T cells developed and proliferated in the absence of WAPL, albeit at a much lower level, the reasons for which remain unclear. One possible explanation is that separation of chromatids during mitosis in T cells may be independent, or only partially dependent, on WAPL, based on their strength and duration of stimulation/activation (Oliveira and Nasmyth, 2013; Srinivasan et al., 2019; Yuen and Gerton, 2018). This notion is consistent with the observation that several cohesinopathies in humans are caused by mutations in various components of cohesin complex and yet do not appear to cause T cell defects (Piché et al., 2019; Remeseiro et al., 2013; Singh and Gerton, 2015). Future studies may determine the role of WAPL and disruption of cohesion in thymopoiesis and in regulation of T cells in secondary lymphoid organs.

The structural changes in our study reflect a polyclonal response from a combination of alloreactive/lymphopenia-induced proliferating cells and the nonproliferating mature T cells. The T cells therefore might be in various stages of early/mid G1, S, G2, M phases. Thus, the genome contact frequency and associated structural changes are reflective of the T cells in these various stages after stimulation. T cells from naïve, syngeneic, and allogeneic settings demonstrated significant changes in internal TAD structure, which were consistent despite the polyclonal nature of the T cell subsets. Nonetheless, although the genome architectures were significantly different, whether these are the direct cause or a consequence of proliferation differences cannot be definitively ascertained. Furthermore, whether antigen-specific T cell responses vary based on the type of antigen cannot be determined from our study. However, our assessment of polyclonal responses is akin to biologically and clinically relevant situations such as allogeneic transplantation.

Our data collectively demonstrate for the first time, to our knowledge, that altering genomic structure *a priori*, at baseline, regulates T cell gene and cellular functions. It is possible that WAPL can regulate expression of genes independent of its effects on genome structure, it is widely held that form precedes function and that genome structure and function are coordinated (Cao et al., 2010; Rajapakse and Groudine, 2011). Mechanistically, the data show that WAPL alters chromatin architecture at cell-cycling genes and therefore links genome structure and function. Nonetheless, validation studies to confirm the exact mechanistic role of WAPL in this context will need to be explored. In addition, although we only validate select cell-cycling genes concomitant with changes in genome structure in this study, it is possible that other cell-cycling genes might be involved in the proliferative defects we observe, and future studies will need to validate these in a systematic manner as well. Future studies may also benefit from integrating single-cell Hi-C and single-cell RNA-seq to refine observations, as features at the TAD and sub-TAD levels observed in this study via bulk Hi-C are a population average and could be variable and distinct between various cell subsets that develop and differentiate after stimulation. Regardless, our data indicate that disruption of 3D chromatin architecture by WAPL may directly regulate gene expression and cellular function of T cells in a physiologically and clinically relevant disease context.

Importantly, we introduce a simple yet robust approach for evaluating TADs and their internal structure. Due to the experimental limitations of performing Hi-C in an *in vivo* setting, we obtained a lower number of cells and thus mappable reads than what Hi-C performed on cell lines or in an *in vitro* setting would typically yield. Consequently, to reliably investigate TAD and sub-TAD level features, we pooled data across all our samples, allowing us to bin our data at a higher resolution. From this pooled matrix, we were able to determine TAD boundaries and subsequently superimpose them onto each sample's raw Hi-C contact map. Informed by this common TAD backbone, we were able to perform targeted analysis of the internal TAD structure in each sample and evaluate how sensitive the backbone and its internal organization are to perturbations across the different settings.

There are no reported cases of isolated germline WAPL mutations in humans (Gard et al., 2009; Piché et al., 2019; Remeseiro et al., 2013; Singh and Gerton, 2015). This is likely because of its critical role during embryonic development. However, somatic mutations in WAPL have been linked to epithelial carcinogenesis (Waldman, 2020). Our study demonstrates that WAPL deficiency in T cells did not cause a profound defect in development of T cells, nor cause T cell malignancy. Thus, WAPL may play a nuanced role in different cell subtypes, depending on their developmental stage, context, and stimulation. Future studies will need to carefully assess the biological implications of WAPL deficiency on T cell subsets and other immune cells. Because WAPL-deficient T cells demonstrated a reduction in GVHD, it is tempting to speculate whether targeting it uniquely in T cells might be a novel strategy to mitigate immunopathologies such as GVHD, allograft rejection, or autoimmunity. Such a strategy may be feasible with emerging gene editing strategies for adoptive transfer of T cells; however, the viability of the strategy to delete WAPL clinically will need significant further investigation. At a broader level, our data provide a proof of concept for the notion that targeting 3D genomic architecture may be a therapeutic strategy that can be potentially harnessed for directly modulating *in vivo* disease processes.

Limitations of study

One challenge we contended with in this study was the low cellular yield for Hi-C resulting from our use of an *in vivo* experimental setting instead of the conventional *in vitro* setting. We anticipate that because of this, contact probabilities for some genomic regions may be underestimated. We believe that analyzing data in an *in vivo* setting, although more clinically relevant, will be an ongoing computational challenge in the Hi-C community and hope to address this limitation in future studies.

We also found read counts between our experimental settings to be highly variable, precluding direct comparison of our baseline (naive) and transplant (syngeneic and allogeneic) T cell contexts. Read counts were more comparable between WT and WAPL knockout (KO) samples, however, allowing us to evaluate differences between WT and KO conditions of naive T cells and differences between WT and KO conditions of syngeneic T cells or of allogeneic T cells. We wish to point out that variable read counts between T cell contexts should not confound such relative comparisons.

STAR★METHODS

Detailed methods are provided in the online version of this paper and include the following:

- KEY RESOURCES TABLE
- RESOURCE AVAILABILITY
 - Lead contact
 - Materials availability
 - Data and code availability
- EXPERIMENTAL MODEL AND SUBJECT DETAILS
 - Mice
 - Generating conditional *Wapl* KO T cells
 - DC isolation and purification
 - T cell isolation and purification, and mixed lymphocyte reaction (MLR)
 - BMT and systemic analyses of GVHD
 - Immunoblotting
 - Study approval
- METHOD DETAILS
 - GVHD and pathology scoring
 - RNA-seq library generation and data processing
 - Generation of Hi-C libraries for sequencing
 - Hi-C data processing
 - Integration of Hi-C and RNA-seq data
 - Frobenius norm
 - Larntz-Perlman procedure
 - A/B compartmentalization
 - Identification of TADs
 - Quantifying internal TAD organization
 - Hi-C derived 5C contact map generation

- Cell proliferation assay
- FxCycle™ Far Red Stain for DNA content measurement
- ELISA
- FACS
- QUANTIFICATION AND STATISTICAL ANALYSIS

SUPPLEMENTAL INFORMATION

Supplemental information can be found online at <https://doi.org/10.1016/j.isci.2022.104846>.

ACKNOWLEDGMENTS

This work is supported by the University of Michigan Genome Science Training Program (GSTP) Fellowship funded by NHGRI under Award Number 5T32HG000040-27 to G.A.D. as well as awards R01HL152605, P01HL149633, and R01CA217156 to P.R.

AUTHOR CONTRIBUTIONS

Conceptualization, P.R. and I.R.; Methodology, Y.S., G.A.D., W.M., I.R., P.R.; Software, G.A.D., S.R.; Validation, Y.S., G.A.D., I.R., P.R.; Formal Analysis, Y.S., G.A.D.; Investigation, Y.S., G.A.D., L.A.M., S.R., K.O.W., D.P. K.S., W.M.; Data Curation, G.A.D.; Writing—Original Draft, Y.S., G.A.D., I.R., P.R.; Writing—Review Editing, Y.S., G.A.D., L.A.M., S.R., K.O.W., D.P. K.S., L.L., W.M., I.R., P.R.; Visualization, Y.S., G.A.D., I.R., P.R.; Supervision, I.R., P.R.; Project Administration, I.R., P.R.; Funding Acquisition, I.R., P.R.

DECLARATION OF INTERESTS

The authors declare no competing interests.

Received: December 6, 2021

Revised: May 10, 2022

Accepted: July 22, 2022

Published: September 16, 2022

REFERENCES

- Allahyar, A., Vermeulen, C., Bouwman, B.A.M., Krijger, P.H.L., Verstegen, M.J.A.M., Geeven, G., van Kranenburg, M., Pieterse, M., Straver, R., Haarhus, J.H.L., et al. (2018). Enhancer hubs and loop collisions identified from single-allele topologies. *Nat. Genet.* **50**, 1151–1160.
- Alvarez, S.E., Harikumar, K.B., Hait, N.C., Allegood, J., Strub, G.M., Kim, E.Y., Maceyka, M., Jiang, H., Luo, C., Kordula, T., et al. (2010). Sphingosine-1-phosphate is a missing cofactor for the e3 ubiquitin ligase traf2. *J. Neurosci. Methods* **465**, 1084–1088.
- Andrews, S., Gilley, J., and Coleman, M.P. (2010). Difference Tracker: ImageJ plugins for fully automated analysis of multiple axonal transport parameters. *J. Neurosci. Methods* **193**, 281–287.
- Bediaga, N.G., Coughlan, H.D., Johanson, T.M., Garnham, A.L., Naselli, G., Schröder, J., Fearnley, L.G., Bandala-Sanchez, E., Allan, R.S., Smyth, G.K., and Harrison, L.C. (2021). Multi-level remodelling of chromatin underlying activation of human t cells. *Sci. Rep.* **11**, 528–616.
- Blazar, B.R., Hill, G.R., and Murphy, W.J. (2020). Dissecting the biology of allogeneic hsc to enhance the gvt effect whilst minimizing gvhd. *Nat. Rev. Clin. Oncol.* **17**, 475–492.
- Bonev, B., and Cavalli, G. (2016). Organization and function of the 3d genome. *Nat. Rev. Genet.* **17**, 661–678.
- Burren, O.S., Rubio García, A., Javierre, B.-M., Rainbow, D.B., Cairns, J., Cooper, N.J., Lambourne, J.J., Schofield, E., Castro Dopico, X., Ferreira, R.C., et al. (2017). Chromosome contacts in activated t cells identify autoimmune disease candidate genes. *Genome Biol.* **18**, 165–219.
- Busslinger, G.A., Stocsits, R.R., Van Der Lelij, P., Axelsson, E., Tedeschi, A., Galjart, N., and Peters, J.-M. (2017). Cohesin is positioned in mammalian genomes by transcription, CTCF and wapl. *Nature* **544**, 503–507.
- Cao, Y., Yao, Z., Sarkar, D., Lawrence, M., Sanchez, G.J., Parker, M.H., MacQuarrie, K.L., Davison, J., Morgan, M.T., Ruzzo, W.L., et al. (2010). Genome-wide myod binding in skeletal muscle cells: a potential for broad cellular reprogramming. *Dev. Cell* **18**, 662–674.
- Chen, H., Chen, J., Muir, L.A., Ronquist, S., Meixner, W., Ljungman, M., Ried, T., Smale, S., and Rajapakse, I. (2015). Functional organization of the human 4d nucleome. *Proc. Natl. Acad. Sci. USA* **112**, 8002–8007.
- Chen, J., Hero, A.O., III, and Rajapakse, I. (2016). Spectral identification of topological domains. *Bioinformatics* **32**, 2151–2158.
- Cremer, M., and Cremer, T. (2019). Nuclear compartmentalization, dynamics, and function of regulatory dna sequences. *Genes Chromosomes Cancer* **58**, 427–436.
- Cremer, T., and Cremer, C. (2001). Chromosome territories, nuclear architecture and gene regulation in mammalian cells. *Nat. Rev. Genet.* **2**, 292–301.
- Cuadrado, A., and Losada, A. (2020). Specialized functions of cohesins stag1 and stag2 in 3d genome architecture. *Curr. Opin. Genet. Dev.* **61**, 9–16.
- Dekker, J., and Mirny, L. (2016). The 3d genome as moderator of chromosomal communication. *Cell* **164**, 1110–1121.
- Dekker, J., Rippe, K., Dekker, M., and Kleckner, N. (2002). Capturing chromosome conformation. *Science* **295**, 1306–1311.
- Dixon, J.R., Selvaraj, S., Yue, F., Kim, A., Li, Y., Shen, Y., Hu, M., Liu, J.S., and Ren, B. (2012). Topological domains in mammalian genomes identified by analysis of chromatin interactions. *Nature* **485**, 376–380.
- Dolatabadi, S., Candia, J., Akrap, N., Vannas, C., Tesan Tomic, T., Losert, W., Landberg, G., Aman, P., and Ståhlberg, A. (2017). Cell cycle and cell size dependent gene expression reveals distinct subpopulations at single-cell level. *Front. Genet.* **8**, 1.
- Dostie, J., Richmond, T.A., Arnaout, R.A., Selzer, R.R., Lee, W.L., Honan, T.A., Rubio, E.D., Krumm, A., Lamb, J., Nusbaum, C., et al. (2006).

- Chromosome conformation capture carbon copy (5c): a massively parallel solution for mapping interactions between genomic elements. *Genome Res.* 16, 1299–1309.
- Drineas, P., and Mahoney, M.W. (2018). Lectures on randomized numerical linear algebra. In *The Mathematics of Data*, p. 25.
- Durand, N.C., Shamim, M.S., Machol, I., Rao, S.S.P., Huntley, M.H., Lander, E.S., and Aiden, E.L. (2016). Juicer provides a one-click system for analyzing loop-resolution hi-c experiments. *Cell Syst.* 3, 95–98.
- Eldén, L. (2007). Matrix Methods in Data Mining and Pattern Recognition (SIAM).
- Finn, E.H., and Misteli, T. (2019). Molecular basis and biological function of variability in spatial genome organization. *Science* 365, eaaw9498.
- Flavahan, W.A., Drier, Y., Liu, B.B., Gillespie, S.M., Venteicher, A.S., Stemmer Rachamimov, A.O., Suvà, M.L., and Bernstein, B.E. (2016). Insulator dysfunction and oncogene activation in *idh* mutant gliomas. *Nature* 529, 110–114.
- Fudenberg, G., Imakaev, M., Lu, C., Goloborodko, A., Abdennur, N., and Mirny, L.A. (2016). Formation of chromosomal domains by loop extrusion. *Cell Rep.* 15, 2038–2049.
- Gard, S., Light, W., Xiong, B., Bose, T., McNairn, A.J., Harris, B., Fleharty, B., Seidel, C., Brickner, J.H., and Gerton, J.L. (2009). Cohesinopathy mutations disrupt the subnuclear organization of chromatin. *J. Cell Biol.* 187, 455–462.
- Goriounov, D., Leung, C.L., and Liem, R.K.H. (2003). Protein products of human *gas2*-related genes on chromosomes 17 and 22 (*hgar17* and *hgar22*) associate with both microfilaments and microtubules. *J. Cell Sci.* 116, 1045–1058.
- Haarhuis, J.H.I., Elbatsh, A.M.O., van den Broek, B., Camps, D., Erkan, H., Jalink, K., Medema, R.H., and Rowland, B.D. (2013). Wapl-mediated removal of cohesin protects against segregation errors and aneuploidy. *Curr. Biol.* 23, 2071–2077.
- Haarhuis, J.H., and Rowland, B.D. (2017). Cohesin: building loops, but not compartments. *EMBO J.* 36, 3549–3551.
- Haarhuis, J.H.I., van der Weide, R.H., Blomen, V.A., Yáñez-Cuna, J.O., Amendola, M., van Ruiten, M.S., Krijger, P.H.L., Teunissen, H., Medema, R.H., van Steensel, B., et al. (2017). The cohesin release factor wapl restricts chromatin loop extension. *Cell* 169, 693–707.e14.
- Hill, L., Ebert, A., Jaritz, M., Wutz, G., Nagasaka, K., Tagoh, H., Kostanova-Poliakova, D., Schindler, K., Sun, Q., Bönel, P., et al. (2020). Wapl repression by *pax5* promotes *v* gene recombination by *igh* loop extrusion. *Nature* 584, 142–147.
- Hu, G., Cui, K., Fang, D., Hirose, S., Wang, X., Wangsa, D., Jin, W., Ried, T., Liu, P., Zhu, J., et al. (2018). Transformation of accessible chromatin and 3d nucleome underlies lineage commitment of early t cells. *Immunity* 48, 227–242.e8.
- Imakaev, M., Fudenberg, G., McCord, R.P., Naumova, N., Goloborodko, A., Lajoie, B.R., Dekker, J., and Mirny, L.A. (2012). Iterative correction of hi-c data reveals hallmarks of chromosome organization. *Nat. Methods* 9, 999–1003.
- Inaba, T., Honda, H., and Matsui, H. (2018). ‘The enigma of monosomy 7’, *Blood*. *Blood* 131, 2891–2898.
- Isoda, T., Moore, A.J., He, Z., Chandra, V., Aida, M., Denholtz, M., Piet van Hamburg, J., Fisch, K.M., Chang, A.N., Fahl, S.P., et al. (2017). Non-coding transcription instructs chromatin folding and compartmentalization to dictate enhancer-promoter communication and t cell fate. *Cell* 171, 103–119.e18.
- Kim, K.-Y., Kovács, M., Kawamoto, S., Sellers, J.R., and Adelstein, R.S. (2005). Disease associated mutations and alternative splicing alter the enzymatic and motile activity of non-muscle myosins ii-b and ii-c. *J. Biol. Chem.* 280, 22769–22775.
- Kim, S.H., McQueen, P.G., Lichtman, M.K., Shevach, E.M., Parada, L.A., and Misteli, T. (2004). Spatial genome organization during t-cell differentiation. *Cytogenet. Genome Res.* 105, 292–301.
- Kueng, S., Hegemann, B., Peters, B.H., Lipp, J.J., Schleiffer, A., Mechtler, K., and Peters, J.-M. (2006). Wapl controls the dynamic association of cohesin with chromatin. *Cell* 127, 955–967.
- Larntz, K., and Perlman, M.D. (1985). ‘A Simple Test for the Equality of Correlation Matrices’, *Rapport Technique* (Department of Statistics, University of Washington), p. 141.
- Le Dily, F., Baù, D., Pohl, A., Vicent, G.P., Serra, F., Soronellas, D., Castellano, G., Wright, R.H.G., Ballare, C., Filion, G., et al. (2014). Distinct structural transitions of chromatin topological domains correlate with coordinated hormone-induced gene regulation. *Genes Dev.* 28, 2151–2162.
- Lieberman-Aiden, E., Van Berkum, N.L., Williams, L., Imakaev, M., Ragozy, T., Telling, A., Amit, I., Lajoie, B.R., Sabo, P.J., Dorschner, M.O., et al. (2009). Comprehensive mapping of long-range interactions reveals folding principles of the human genome. *Science* 326, 289–293.
- Lindsly, S., Chen, C., Liu, S., Ronquist, S., Dilworth, S., Perlman, M., and Rajapakse, I. (2021). 4dnvestigator: time series genomic data analysis toolbox. *Nucleus* 12, 58–64.
- Liu, N.Q., Maresca, M., van den Brand, T., Braccioli, L., Schijns, M.M.G.A., Teunissen, H., Bruneau, B.G., Nora, E.P., and de Wit, E. (2021). Wapl maintains a cohesin loading cycle to preserve cell-type-specific distal gene regulation. *Nat. Genet.* 53, 100–109.
- Lupiáñez, D.G., Kraft, K., Heinrich, V., Krawitz, P., Brancati, F., Klopocki, E., Horn, D., Kayserili, H., Opitz, J.M., Laxova, R., et al. (2015). Disruptions of topological chromatin domains cause pathogenic rewiring of gene-enhancer interactions. *Cell* 161, 1012–1025.
- Maeda, Y., Tawara, I., Teshima, T., Liu, C., Hashimoto, D., Matsuoka, K.-I., Tanimoto, M., and Reddy, P. (2007). Lymphopenia-induced proliferation of donor t cells reduces their capacity for causing acute graft-versus-host disease. *Exp. Hematol.* 35, 274–286.
- Misteli, T. (2020). The self-organizing genome: principles of genome architecture and function. *Cell* 183, 28–45.
- Nasmyth, K., and Haering, C.H. (2009). Cohesin: its roles and mechanisms. *Annu. Rev. Genet.* 43, 525–558.
- Nora, E.P., Lajoie, B.R., Schulz, E.G., Giorgetti, L., Okamoto, I., Servant, N., Piolot, T., Van Berkum, N.L., Meisig, J., Sedat, J., et al. (2012). Spatial partitioning of the regulatory landscape of the x-inactivation centre. *Nature* 485, 381–385.
- Oliveira, R.A., and Nasmyth, K. (2013). Cohesin cleavage is insufficient for centriole disengagement in drosophila. *Curr. Biol.* 23, R601–R603.
- Peters, J.-M., and Nishiyama, T. (2012). Sister chromatid cohesion. *Cold Spring Harbor Perspect. Biol.* 4, a011130.
- Piché, J., Van Vliet, P.P., Pucéat, M., and Andelfinger, G. (2019). The expanding phenotypes of cohesinopathies: one ring to rule them all. *Cell Cycle* 18, 2828–2848.
- Rajapakse, I., and Groudine, M. (2011). On emerging nuclear order. *J. Cell Biol.* 192, 711–721.
- Rajapakse, I., Groudine, M., and Mesbahi, M. (2011). Dynamics and control of stadedependent networks for probing genomic organization. *Proc. Natl. Acad. Sci. USA* 108, 17257–17262.
- Ran, F.A., Cong, L., Yan, W.X., Scott, D.A., Gootenberg, J.S., Kriz, A.J., Zetsche, B., Shalem, O., Wu, X., Makarova, K.S., et al. (2015). *In vivo* genome editing using staphylococcus aureus cas9. *Nature* 520, 186–191.
- Rao, S.S.P., Huntley, M.H., Durand, N.C., Stamenova, E.K., Bochkov, I.D., Robinson, J.T., Sanborn, A.L., Machol, I., Omer, A.D., Lander, E.S., and Aiden, E.L. (2014). A 3d map of the humangenome at kilobase resolution reveals principles of chromatin looping. *Cell* 159, 1665–1680.
- Rawlings, J.S., Gatzka, M., Thomas, P.G., and Ihle, J.N. (2011). Chromatin condensation via the condensin ii complex is required for peripheral t-cell quiescence. *EMBO J.* 30, 263–276.
- Reddy, P., Negrin, R., and Hill, G.R. (2008). Mouse models of bone marrow transplantation. *Biol. Blood Marrow Transplant.* 14, 129–135.
- Remeseiro, S., Cuadrado, A., and Losada, A. (2013). Cohesin in development and disease. *Development* 140, 3715–3718.
- Robinson, J.T., Thorvaldsdóttir, H., Winckler, W., Guttman, M., Lander, E.S., Getz, G., and Mesirov, J.P. (2011). Integrative genomics viewer. *Nat Biotechnol.* 29, 24–26.
- Robson, M.I., de Las Heras, J.I., Czapiewski, R., Sivakumar, A., Kerr, A.R.W., and Schirmer, E.C. (2017). Constrained release of lamina-associated enhancers and genes from the nuclear envelope during t-cell activation facilitates their association in chromosome compartments. *Genome Res.* 27, 1126–1138.
- Schwarzer, W., Abdennur, N., Goloborodko, A., Pekowska, A., Fudenberg, G., Loe-Mie, Y.,

- Fonseca, N.A., Huber, W., Haering, C.H., Mirny, L., and Spitz, F. (2017). Two independent modes of chromatin organization revealed by cohesin removal. *Nature* 551, 51–56.
- Seitan, V.C., Hao, B., Tachibana-Konwalski, K., Lavagnoli, T., Mira-Bontenbal, H., Brown, K.E., Teng, G., Carroll, T., Terry, A., Horan, K., et al. (2011). A role for cohesin in T-cell-receptor rearrangement and thymocyte differentiation. *Nature* 476, 467–471.
- Shen, Y., Yue, F., McCleary, D.F., Ye, Z., Edsall, L., Kuan, S., Wagner, U., Dixon, J., Lee, L., Lobanenko, V.V., and Ren, B. (2012). A map of the cis-regulatory sequences in the mouse genome. *Nature* 488, 116–120.
- Silva, M.C.C., Powell, S., Ladstätter, S., Gassler, J., Stocsits, R., Tedeschi, A., Peters, J.-M., and Tachibana, K. (2020). Wapl releases scc1-cohesin and regulates chromosome structure and segregation in mouse oocytes. *J. Cell Biol.* 219, e201906100.
- Singh, V.P., and Gerton, J.L. (2015). Cohesin and human disease: lessons from mouse models. *Curr. Opin. Cell Biol.* 37, 9–17.
- Srinivasan, M., Petela, N.J., Scheinost, J.C., Collier, J., Voulgaris, M., B Roig, M., Beckouët, F., Hu, B., and Nasmyth, K.A. (2019). Scc2 counteracts a wapl-independent mechanism that releases cohesin from chromosomes during g1. *Elife* 8, e44736.
- Straight, A.F., Cheung, A., Limouze, J., Chen, I., Westwood, N.J., Sellers, J.R., and Mitchison, T.J. (2003). Dissecting temporal and spatial control of cytokinesis with a myosin ii inhibitor. *Science* 299, 1743–1747.
- Strang, G., Strang, G., Strang, G., and Strang, G. (1993). *Introduction to Linear Algebra*, 3 (Wellesley-Cambridge Press Wellesley).
- Subramanian, A., Kuehn, H., Gould, J., Tamayo, P., and Mesirov, J.P. (2007). GSEA-P: a desktop application for gene set enrichment analysis. *Bioinformatics* 23, 3251–3253.
- Sun, Y., Oravec-Wilson, K., Bridges, S., McEachin, R., Wu, J., Kim, S.H., Taylor, A., Zajac, C., Fujiwara, H., Peltier, D.C., et al. (2019). mir-142 controls metabolic reprogramming that regulates dendritic cell activation. *J. Clin. Invest.* 129, 2029–2042.
- Sun, Y., Oravec-Wilson, K., Mathewson, N., Wang, Y., McEachin, R., Liu, C., Toubai, T., Wu, J., Rossi, C., Braun, T., et al. (2015). Mature t cell responses are controlled by microrna 142. *J. Clin. Invest.* 125, 2825–2840.
- Sun, Y., Tawara, I., Zhao, M., Qin, Z.S., Toubai, T., Mathewson, N., Tamaki, H., Nieves, E., Chinnaiyan, A.M., Reddy, P., et al. (2013). Allogeneic t cell responses are regulated by a specific mirna-mrna network. *J. Clin. Invest.* 123, 4739–4754.
- Szabo, Q., Bantignies, F., and Cavalli, G. (2019). Principles of genome folding into topologically associating domains. *Sci. Adv.* 5, eaaw1668.
- Tabebordbar, M., Zhu, K., Cheng, J.K.W., Chew, W.L., Widrick, J.J., Yan, W.X., Maesner, C., Wu, E.Y., Xiao, R., Ran, F.A., et al. (2016). In vivo gene editing in dystrophic mouse muscle and muscle stem cells. *Science* 351, 407–411.
- Tedeschi, A., Wutz, G., Huet, S., Jaritz, M., Wuensche, A., Schirghuber, E., Davidson, I.F., Tang, W., Cisneros, D.A., Bhaskara, V., et al. (2013). Wapl is an essential regulator of chromatin structure and chromosome segregation. *Nature* 501, 564–568.
- Trapnell, C., Williams, B.A., Pertea, G., Mortazavi, A., Kwan, G., van Baren, M.J., Salzberg, S.L., Wold, B.J., and Pachter, L. (2010). ‘Transcript assembly and quantification by RNA-Seq reveals unannotated transcripts and isoform switching during cell differentiation’, 1061. *Nat. Biotechnol.* 28, 511–515.
- Tsuruga, H., Yabuta, N., Hashizume, K., Ikeda, M., Endo, Y., and Nojima, H. (1997). Expression, nuclear localization and interactions of human mcm/p1 proteins. *Biochem. Biophys. Res. Commun.* 236, 118–125.
- Waldman, T. (2020). Emerging themes in cohesin cancer biology. *Nat. Rev. Cancer* 20, 504–515.
- Wu, S.-R., and Reddy, P. (2017). ‘Tissue tolerance: a distinct concept to control acute GVHD severity. *Blood* 129, 1747–1752.
- Wutz, G., Várnai, C., Nagasaka, K., Cisneros, D.A., Stocsits, R.R., Tang, W., Schoenfelder, S., Jessberger, G., Muhar, M., Hossain, M.J., et al. (2017). Topologically associating domains and chromatin loops depend on cohesin and are regulated by ctcf, wapl, and pds5 proteins. *EMBO J.* 36, 3573–3599.
- Yang, J., McGovern, A., Martin, P., Duffus, K., Ge, X., Zarrineh, P., Morris, A.P., Adamson, A., Fraser, P., Rattray, M., and Eyre, S. (2020). Analysis of chromatin organization and gene expression in t cells identifies functional genes for rheumatoid arthritis. *Nat. Commun.* 11, 4402–4413.
- Yuen, K.C., and Gerton, J.L. (2018). Taking cohesin and condensin in context. *PLoS Genet.* 14, e1007118.
- Zeiser, R., and Blazar, B.R. (2017). Acute graft-versus-host disease—biologic process, prevention, and therapy. *N. Engl. J. Med.* 377, 2167–2179.

STAR★METHODS

KEY RESOURCES TABLE

REAGENT or RESOURCE	SOURCE	IDENTIFIER
Antibodies		
anti-Wapl rabbit polyclonal Ab	Proteintech group Rosemont, IL	#16370-1-AP
anti-β-actin mouse mAb	Abcam Waltham, MA	ab8226
rat Anti-Mouse CD16/CD32	BD Pharmingen™ San Diego, CA	#553142
anti-mouse CD4 APC	BioLegends San Diego, CA	#100412
anti-mouse CD8 APC	BioLegends San Diego, CA	#100712
anti-mouse CD3 APC	BioLegends San Diego, CA	#100312
anti-mouse CD45.2 APC	BioLegends San Diego, CA	#109814
anti-mouse CD45.1 APC	BioLegends San Diego, CA	#110714
anti-mouse CD25 APC	BioLegends San Diego, CA	#102012
anti-mouse CD69 APC	BioLegends San Diego, CA	#104514
anti-mouse CD3 PE	BioLegends San Diego, CA	#100206
anti-mouse CD4 PE	BioLegends San Diego, CA	#100512
anti-mouse CD8a PE	BioLegends San Diego, CA	#100708
anti-mouse CD25 PE	BioLegends San Diego, CA	#102008
anti-mouse TCR β PE	BioLegends San Diego, CA	#109208
anti-mouse CD3 PerCP/Cyanine5.5	BioLegends San Diego, CA	#100218
anti-mouse CD4 PerCP/Cyanine5.5	BioLegends San Diego, CA	#100434
anti-mouse CD8a PerCP/Cyanine5.5	BioLegends San Diego, CA	#100734
Mouse anti-rabbit IgG-HRP	Santa Cruz Biotechnology Santa Cruz, CA	SC-2357
Mouse-IgGk BP-HRP	Santa Cruz Biotechnology Santa Cruz, CA	SC-516102
Mouse anti- FoxP3 antibody PE	eBioscience, San Diego, CA	#126403
PE Annexin V	BioLegends San Diego, CA	#640934
Chemicals, peptides, and recombinant proteins		
H ³ -Thymidine	Perkin Elmer	NET027005MC
CellTrace™ Far Red	Invitrogen	C34564
Dynabeads Mouse T-Activator CD3/CD28	Gibco	11452D
FxCycle™ Far Red Stain	Invitrogen	F10348
RNase A	Roche	#70294823
anti-CD90.2 microbeads	Miltenyi Biotec Inc., Auburn, CA	#130-121-278
CD11 c MicroBeads	Miltenyi Biotec Inc., Auburn, CA	#130-108-338
Miltenyi LS Columns	Miltenyi Biotec Inc., Auburn, CA	#130-042-401
PVDF membrane	Thermo Scientific Rockford IL	#88518
IGEPAL® CA-630	MilliporeSigma Burlington, MA	#9002-93-1
Protease Inhibitor Cocktail powder	MilliporeSigma Burlington, MA	P2714
Sodium dodecyl sulfate	Sigma-Aldrich St. Louis, MO	#436143
Triton™ X-100	Sigma-Aldrich St. Louis, MO	#9036-19-5
Restriction enzyme Mbol	NEB Ipswich, MA	R0147S
Biotin-14-dATP	ThermoFisher Scientific, Ann Arbor, MI	#19524016
DNA Polymerase I, Large (Klenow) Fragment	NEB Ipswich, MA	M0210S
T4 DNA Ligase	NEB Ipswich, MA	M0202S
Proteinase K	NEB Ipswich, MA	P8107S

(Continued on next page)

Continued

REAGENT or RESOURCE	SOURCE	IDENTIFIER
Dynabeads™ MyOne™ Streptavidin C1	ThermoFisher Scientific, Ann Arbor, MI	#65002
T4 Polynucleotide Kinase	NEB Ipswich, MA	M0201L
T4 DNA Polymerase	NEB Ipswich, MA	M0203L
Klenow Fragment (3' → 5' exo-)	NEB Ipswich, MA	M0212L
PfuUltra II Fusion High-fidelity DNA Polymerase	Agilent Technologies, Inc Santa Clara, CA	#600387
IC Fixation Buffer	Biolegend San Diego, CA	#420801
Permeabilization Buffer	Biolegend San Diego, CA	#421002

Critical commercial assays

Pan T Cell Isolation Kit II	Miltenyi Biotec Inc., Auburn, CA	#130-095-130
IFNg DuoSet ELISA Kit	BD Systems	DY485
TNFalpha ELISA Set	BD OptEIAMT	555268
Pierce™ ECL Western	Thermo Scientific Rockford IL	#32106
AMPure XP beads	Beckman Coulter Indianapolis IN	C63510
LIVE/DEAD™ Fixable Far Red Dead Cell Stain Kit	ThermoFisher Scientific, Ann Arbor, MI	L10120
AllPrep DNA/RNA Mini Kit	Qiagen Germantown, MD	#80204

Deposited data

RNA-seq mouse donor T-cells 7 days post HSCT	This paper	GEO: GSE134975.
T cell chromosome architecture (Hi-C)	This paper	BioProject PRJNA608895

Experimental models: Organisms/strains

C57BL/6, H2b genotype	Charles River Labs; Mattawan, Michigan	Strain Code: 027
Rosa26-floxed STOP-Cas9 knockin	The Jackson Laboratory	Stock No:026175
CD4-Cre	The Jackson Laboratory	Stock No: 017336
BALB/c, H2d genotype	Charles River Labs; Mattawan, Michigan	Strain Code: 028

Oligonucleotides

Forward primer to determine sgRNA insertion (Wapl-F): 5'-CCGTAAGATGAACCCTTACCC	This paper	N/A
Reverse primer to determine sgRNA insertion (Wapl-R): 5'-TCTGAGTAAGATCGGTGTTTCG	This paper	N/A
Forward primer to determine if CD4-Cre exists (CD4CRE-F): 5'-GACATGTTCAAGGATCGCCA	This paper	N/A
Reverse primer to determine if CD4-Cre exists (CD4CRE-R): 5'-AACCAGCGTTTTCTGTTCTGC	This paper	N/A
Forward primer to determine stop sign cleavage (LSL-F): 5'-GCAACGTGCTGGTTATTGTG	This paper	N/A
Reverse primer to determine stop sign cleavage (LSL-R): 5'-TAGTCTCCGTCGTGGTCCTT	This paper	N/A
Forward primer to check Gas2l1 expression (Gas2l1-F): 5'-CGAGCTACCCCTCAG GTTTC-3'	This paper	N/A

(Continued on next page)

Continued

REAGENT or RESOURCE	SOURCE	IDENTIFIER
Reverse primer to check Gas2l1 expression (Gas2l1-R): 5'-CTGGAGTCTCCCACTCGGTA-3'	This paper	N/A
Forward primer to check Mcm3 expression (Mcm3-F): 5'-AAGAAGGGCTGCTACACCTC-3'	This paper	N/A
Reverse primer to check Mcm3 expression (Mcm3-R): 5'-CCGTTTTCAAGTCCCGCTC-3'	This paper	N/A
Forward primer to check Sphk1 expression (Sphk1-F): 5'-ACTCACCGAACGGAAGAACC-3'	This paper	N/A
Reverse primer to check Sphk1 expression (Sphk1-R): 5'-AGCAGTTCATGGGTGACAG-3'	This paper	N/A
Forward primer to check Myh10 expression (Myh10 -F): 5'-GCTTGAACGAAGCCTCTGTCT-3'	This paper	N/A
Reverse primer to check Myh10 expression (Myh10 -R): 5'-CGTGGCAAGGTACTGAATGA-3'	This paper	N/A

Recombinant DNA

pX330-U6-Chimeric_BB-CBh-hSpCas9	Addgene Watertown, MA	#42230
----------------------------------	-----------------------	--------

Software and algorithms

FastQC	Andrews et al., 2010	https://www.bioinformatics.babraham.ac.uk/projects/fastqc/
RNA-Seq Alignment v1.0	Illumina, Inc.	https://www.illumina.com/products/by-type/informatics-products/basespace-sequence-hub/apps/ma-seq-alignment.html
Cufflinks v.2.2.1	Trapnell et al. (2010)	https://cole-trapnell-lab.github.io/cufflinks/
Integrative Genomics Viewer (IGV)	Robinson et al. (2011)	https://software.broadinstitute.org/software/igv/
Gene Set Enrichment Analysis (GSEA)	Subramanian et al., 2007	https://www.gsea-msigdb.org/gsea/index.jsp
4DNvestigator	Lindsay et al. (2021)	https://github.com/lindsay/4DNvestigator

RESOURCE AVAILABILITY

Lead contact

Further information and requests for resources, reagents and strains should be directed to and will be fulfilled by the lead contact, Pavan Reddy (reddypr@umich.edu).

Materials availability

The mouse strain generated in this study is available from the [lead contact](#) with a completed Materials Transfer Agreement.

Data and code availability

RNA-seq and Hi-C data have been deposited at GEO and BioProject, respectively, and are publicly available. Accession numbers are listed in the [key resources table](#). This paper does not report original code. Any additional information required to reanalyze the data reported in this paper is available from the [lead contact](#) upon request.

EXPERIMENTAL MODEL AND SUBJECT DETAILS

Mice

B6 (H2b, CD4.1 and CD45.2), BALB/c (H2d, CD45.1 and CD45.2), Rosa26-floxed STOP Cas9 knockin (B6J) and CD4CRE (B6) mice were purchased from The Jackson Laboratory and the National Cancer Institute. The ages of the mice used for experiments ranged between 8 and 12 weeks. Mice were housed in sterilized microisolator cages and received filtered water and normal chow.

Generating conditional *Wapl* KO T cells

We designed 2 sgRNAs targeting exon 2 of the *Wapl* locus which are localized in mouse Chromosome 14 qB (Figure S3) (Ran et al., 2015). Three lines of mice with B6 background were used to generate conditional *Wapl* KO mice in T cells. The first line was generated to carry CRISPR-sgRNAs targeting insert to identify exon 2 in *Wapl* (Figure 1A). The second and third lines are Rosa26-floxed STOP-Cas9-GFP knockin on B6J (The Jackson Laboratory, Stock No:026175) and CD4-CRE transgenic mice (The Jackson Laboratory, Stock No: 017336). Tail DNA was screened for a positive sgRNAs-*Wapl* insert, positive CRE, and a stop signal in loxP-SV40pA x3-loxP cleavage or deletion. The potential *Wapl* KO T cells were sorted for positive GFP (Figure 1B). To confirm the success of conditional in KO in T cells, T cells were processed for SDS-PAGE and detected with anti-*Wapl* antibody. Additionally, total RNAs were isolated from *Wapl* KO and WT T cells and processed for RNA-seq.

DC isolation and purification

Dendritic cells (DC) were isolated from splenocytes either from WT B6 or BALB/c mice. Single-cell suspensions were prepared according to the manufacturer's instruction then subjected to CD11c microbead (MACS) staining and positive selection using LS column (MiltenyiBiotec). The purity of enriched CD11c⁺ DC preparation was 85.6–90%.

T cell isolation and purification, and mixed lymphocyte reaction (MLR)

WT and *Wapl* KO B6 T cells were isolated by negative selection (>95% purity) (Pan T Cell Isolation Kit II; Miltenyi Biotec). T cells were co-cultured with B6 WT or BALB/c DCs at a ratio of 40:1 (T cells versus DCs $3 \times 10^5:7.5 \times 10^3$) for 96 h using 96-well flat-bottomed plates (Falcon Labware), or stimulated with Dynabeads T cell activator CD3/CD28 (25 ul/106/mL) for 2 or 3 days respectively. Proliferation was determined by incubating the cells with H³-thymidine (1 Ci/well [0.037 MBq]) for the last 20 or 6 h, respectively. H³-thymidine incorporation in T cells was counted on a 1205 Betaplate reader (Wallac, Turku, Finland).

BMT and systemic analyses of GVHD

Bone marrow transplantations (BMTs) were performed. The donor T cells (WT B6 or WAPL deficiency) were isolated from spleens and purified by negative selection (using the Pan T cell Isolation Kit II; Miltenyi Biotec). Bone marrow cells from tibia and fibula were harvested and TCD (T cell deletion) BM cells were isolated with positive selection using anti-CD90.2 microbeads and LS column (Miltenyi Biotec). The recipient BALB/c mice received an 800-cGy total body irradiation on day -1 (split dose) and T cells (1×10^6 , either B6 WT or WAPL deficiency T cells, and TCD BM cells (5×10^6 , from WT B6 mice) were injected intravenously into the recipients on day 0. The syngeneic B6 control mice received a 1000-cGy total body irradiation on day -1. T cells (2×10^6 , isolated from B6 WT mice) and TCD BM cells (5×10^6 from B6 WT mice) were injected intravenously into the recipients on day 0. Mice were housed in sterilized microisolator cages and received normal chow and autoclaved hyperchlorinated drinking water for the first 3 weeks after BMT.

Immunoblotting

T cell lysates were extracted as previously described (Sun et al., 2015), and 50 to 100 g of protein extract was separated in SDS-PAGE and transferred onto a PVDF membrane (GE Health care). The membrane was blocked with 5% nonfat milk for 30 min and then incubated overnight at 4 °C with the following Abs in 5% nonfat milk: anti-*Wapl* rabbit polyclonal Ab (1:500 in nonfat milk, Proteintech Cat 16370-1-AP), anti- β -actin mouse mAb (1:1,000 in 5% nonfat milk; Abcam, catalog ab8226). After washing 3 times with TBST for 5 min, the blot was incubated with specific HRP-labeled secondary Ab, washed again with TBST, and signal generated and visualized using the Enhanced Chemiluminescence Kit (Thermo Scientific, Cat 32106).

Study approval

Study approval. All animal studies were reviewed and approved by the University Committee on Use and Care of Animals of the University of Michigan, based on University Laboratory Animal Medicine guidelines.

METHOD DETAILS

GVHD and pathology scoring

Survival was monitored daily. The degree of systemic GVHD was assessed by a standard scoring system with four criteria scores: percentage of weight change, posture, activity, fur texture, and skin integrity, and subsequently graded from 0 to 2 for each criterion (maximum index = 10) (Sun et al., 2015). Acute GVHD was also assessed by histopathologic analysis of the ileum and the ascending colon, liver, and ear skin. Specimens were harvested from animals on day 21 after BMT, then processed and stained with hematoxylin and eosin. Coded slides were examined systematically in a blind manner by using a semi-quantitative scoring system to assess the following abnormalities known to be associated with GVHD, small intestine: villous blunting, crypt regeneration, loss of enterocyte brush border, luminal sloughing of cellular debris, crypt cell apoptosis, outright crypt destruction, and lamina propria lymphocytic infiltrate; colon: crypt regeneration, surface colonocytes, colonocyte vacuolization, surface colonocyte attenuation, crypt cell apoptosis, outright crypt destruction, and lamina propria lymphocytic infiltrate; liver: portal tract expansion, neutrophil infiltrate, mononuclear cell infiltrate, nuclear pleomorphism, intraluminal epithelial cells, endothelialitis, hepatocellular damage, acidophilic bodies, mitotic figures, neutrophil accumulations, macrophage aggregates, macrocytosis; skin: apoptosis in epidermal basal layer or lower malpighian layer or outer root sheath of hair follicle or acrosyringium, lichenoid inflammation, vacuolar change, lymphocytic satellitosis. The scoring system denoted 0 as normal, 0.5 as focal and rare, 1.0 as focal and mild, 2.0 as diffuse and mild, 3.0 as diffuse and moderate, and 4.0 as diffuse and severe. Scores were summed together to provide a total score for each specimen (Sun et al., 2015).

RNA-seq library generation and data processing

Näive WT and *Wapl* KO T cells, or WT and *Wapl* KO T cells isolated from syngeneic or allogeneic BMT on day 7 were first purified as described previously (Sun et al., 2015). All dead cells were excluded by sorting for far-red fluorescent reactive dye (Invitrogen, Cat. L10120). Then, WT T cells were sorted for PE-CD3 and APC-CD45.2 while *Wapl* KO T cells were sorted for APC-CD3, PE-CD45.2 and positive GFP. Each sample contained pooled T cells from 3-4 mice, and samples in each group were biologically triplicated. RNA was isolated using DNA/RNA mini Kit (Qiagen Cat 80204) by following the RNA isolation procedures. Sequencing was performed by the University of Michigan (UM) DNA Sequencing Core, using the Illumina Hi-Seq 4000 platform, paired-end, 50 cycles and Ribosomal Reduction library prep.

We obtained read files from the UM Sequencing Core and concatenated those into a single FASTQ file for each sample. We checked the quality of the raw read data for each sample using FastQC (version 0.11.3) to identify features of the data that may indicate quality problems (e.g., low quality scores, overrepresented sequences, inappropriate GC content). We used the Tuxedo Suite software package for alignment, differential expression analysis, and post-analysis diagnostics. Briefly, we aligned reads to the reference genome (GRCm38) using TopHat (version 2.0.13) and Bowtie2 (version 2.2.1). We used default parameter settings for alignment, with the exception of: “-b2-very-sensitive” telling the software to spend extra time searching for valid alignments. We used FastQC for a second round of quality control (post-alignment), to ensure that only high quality data would be input to expression quantitation and differential expression analysis. We used Cufflinks/CuffDiff (version 2.2.1) for expression quantitation, normalization, and differential expression analysis, using GRCm38.fa as the reference genome sequence. For this analysis, we used parameter settings: “-multi-read-correct” to adjust expression calculations for reads that map in more than one locus, as well as “-compatible-hits-norm” and “-upper-quartile norm” for normalization of expression values. We generated diagnostic plots using the CummeRbund R package. We used locally developed scripts to format and annotate the differential expression data output from CuffDiff. Briefly, we identified genes and transcripts as being differentially expressed based on FDR 0.05, and fold change \pm 1.5. We annotated genes with NCBI Entrez GeneIDs and text descriptions. RNA-seq reads in bam format were mapped to the most recent mouse genome (mm10) using the Integrative Genomics Viewer (IGV). The RNA-seq data reported here can be found in the Gene Expression Omnibus (GEO) database with the series accession ID GSE134975.

Generation of Hi-C libraries for sequencing

The *in situ* Hi-C protocols from Rao et al. (2014) were adapted with slight modifications. For each Hi-C library, approximately 1×10^6 cells were incubated in 250 μ L of ice-cold Hi-C lysis buffer (10 mM Tris-HCl pH8.0, 10 mM NaCl, 0.2% Igepal CA630) with 50 μ L of protease inhibitors (Sigma) on ice for 30 min and washed with 250 μ L lysis buffer. The nuclei were pelleted by centrifugation at 2500 \times g for 5 min at 4°C, re-suspended in 50 μ L of 0.5% sodium dodecyl sulfate (SDS) and incubated at 62°C for 10 minutes. Afterwards 145 μ L of water and 25 μ L of 10% Triton X-100 (Sigma) were added and incubated at 37°C for 15 min.

Chromatin was digested with 200 units of restriction enzyme Mbol (NEB) overnight at 37°C with rotation. Chromatin end overhangs were filled in and marked with biotin-14-dATP (Thermo Fisher Scientific) by adding the following components to the reaction: 37.5 μ L of 0.4 mM biotin-14-dATP (Life Technologies), 1.5 μ L of 10 mM dCTP, 1.5 μ L of 10 mM dGTP, 1.5 μ L of 10 mM dTTP, and 8 μ L of 5 U/ μ L DNA Polymerase I, Large (Klenow) Fragment (NEB). The marked chromatin ends were ligated by adding 900 μ L of ligation master mix consisting of 663 μ L of water, 120 μ L of 10X NEB T4 DNA ligase buffer (NEB), 100 μ L of 10% Triton X-100, 12 μ L of 10 mg/mL BSA, 5 μ L of 400 U/ μ L T4 DNA Ligase (NEB), and incubated at room temperature for 4 h.

Chromatin de-crosslinking was performed by adding 50 μ L of 20 mg/mL proteinase K (NEB) and 120 μ L of 10% SDS and incubated at 55 °C for 30 min, adding 130 μ L of 5 M sodium chloride and incubate at 68°C overnight. DNA was precipitated with ethanol, washed with 70% ethanol, and dissolved in 105 μ L of 10 mM Tris-HCl, pH 8. DNA was sheared on a Covaris S2 sonicator. Biotinylated DNA fragments were pulled with the MyOne Streptavidin C1 beads (Life Technologies). To repair the ends of sheared DNA and remove biotin from unligated ends, DNA-bound beads were re-suspended in 100 μ L of mix containing 82 μ L of 1X NEB T4 DNA ligase buffer with 10 mM ATP (NEB), 10 μ L of 10 (2.5 mM each) 25 mM dNTP mix, 5 μ L of 10 U/ μ L NEB T4 PNK (NEB), 4 μ L of 3 U/ μ L NEB T4 DNA polymerase (NEB), and 1 μ L of 5 U/ μ L NEB DNA polymerase I, Large (Klenow) Fragment (NEB).

After end-repair, dATP attachment was carried out in 100 μ L of reaction solution, consisting of 90 μ L of 1X NEBuffer 2, 5 μ L of 10 mM dATP, and 5 μ L of 5 U/ μ L NEB Klenow exo minus (NEB). The reaction was incubated at 37°C for 30 min. The beads were then cleaned for Illumina sequencing adaptor ligation which was done in a mix containing 50 μ L of 1X T4 ligase buffer, 3 μ L T4 DNA ligases (NEB), and 2 μ L of a 15 μ M Illumina indexed adapter at room temperature for 1 h. DNA was dissociated from the bead by heating at 98 °C for 10 min, separated on a magnet, and transferred to a clean tube.

Final amplification of the library was carried out in multiple PCRs using Illumina PCR primers. The reactions were performed in 25 μ L scale consisting of 25 ng of DNA, 2 μ L of 2.5 mM dNTPs, 0.35 μ L of 10 μ M each primer, 2.5 μ L of 10X PfuUltra buffer, PfuUltra II Fusion DNA polymerase (Agilent). The PCR cycle conditions were set to 98°C for 30 s as the denaturing step, followed by 14 cycles of 98°C 10 s, 65°C for 30 s, 72°C for 30 s, then with an extension step at 72°C for 7 min.

After PCR amplification, the products from the same library were pooled and fragments ranging in size from 300 to 500 bp were selected with AMPure XP beads (Beckman Coulter). The size-selected libraries were sequenced to produce paired-end Hi-C reads on the Illumina HiSeq 2500 platform with the V4 of 125 cycles.

Hi-C data processing

We generated the Hi-C matrices using Juicer (Durand et al., 2016). Juicer uses BWA-mem to align each paired-end read separately. It then determines which reads can be mapped uniquely and keeps unambiguously mapped read pairs. Each read is assigned to a "fragment", determined by the restriction enzyme cut sites and paired reads that map to the same fragment are removed. The Juicer pipeline creates a binary data file (namely, the ".hic" file), which contains Hi-C contacts. The .hic file is imported into MATLAB-compatible variables via our in-house MATLAB toolbox, 4DNvestigator (Lindsly et al., 2021). Centromeric and telomeric regions were removed in the process. Then, Hi-C data were subsequently normalized and binned at 50 and 100 kb resolution. ICE (Imakaev et al., 2012) and "observed over expected" (O/E) normalized contact maps at 100 kb resolution were used for chromosome-level analysis of A/B compartments. Observed contact maps at 50 kb resolution were used for detection and analysis of TADs. Hi-C data for this study are available through the NCBI BioProject database (accession number: PRJNA608895).

Integration of Hi-C and RNA-seq data

To integrate our Hi-C and RNA-seq datasets, we first binned measurements at the same resolution. Accordingly, each element in the binned RNA-seq expression vector corresponds to a row (or column) of the Hi-C contact matrix that captures the same set of genomic loci. Genomic bins spanning a given region contain measurements reflecting the sum of its parts, where expression values for genes sharing the same bin are summed and contact frequencies for loci occupying the same bin are summed. This allows us to directly compare the transcriptional and conformational behavior across regions of the genome.

Frobenius norm

The Frobenius norm describes the size or volume of a matrix (Strang et al., 1993). As such, the Frobenius norm can be used as a measure of variance or variability in data (Drineas and Mahoney, 2018). For matrix A of dimension m , that is $A \in \mathbb{R}^{m \times n}$, the mathematical definition of the Frobenius norm is as follows:

$$\|A\|_F = \sqrt{\sum_{i=1}^m \sum_{j=1}^n a_{ij}^2}, \quad (\text{Equation 1})$$

where a_{ij} is an element of the data matrix A . Equivalently this expression can be written as.

$$\|A\|_F^2 = \text{trace}(A^T A), \quad (\text{Equation 2})$$

where *trace* is the sum of the diagonal elements of a matrix (Eldén, 2007). When comparing two sets of data, the notation can be modified as follows:

$$\|A - B\|_F^2 = \text{trace}\left((A - B)^T (A - B)\right), \quad (\text{Equation 3})$$

where A and B are matrices of the same dimensions. The Frobenius norm of a vector is equivalent to the Euclidean norm.

Larntz-Perlman procedure

The Larntz-Perlman (LP) procedure is a method designed to test the equivalence of correlation matrices (Larntz and Perlman, 1985). We applied the LP procedure as described in the 4DNinvestigator Toolbox (Lindsly et al., 2021) to compare Hi-C contact matrices between WT and *Wapl* KO conditions. Briefly, correlation matrices are derived from data by taking the pair-wise linear correlation coefficient between each pair of columns in the Hi-C contact matrices. Then, a null hypothesis is defined from corresponding population correlation matrices. We then compute a Fisher z-transformation on the correlation matrices and calculate a test statistic for the chi-squared distribution to determine whether or not the null hypothesis (that Hi-C matrices are equivalent) should be rejected with a corresponding p-value.

A/B compartmentalization

Chromatin can either take on a condensed heterochromatic form or a looser euchromatic form. We use the Fiedler vector – the eigenvector corresponding to the second smallest eigenvalue (Fiedler number) of the normalized Laplacian matrix – to describe this feature mathematically which allows us to bi-partition the data into signed compartments – “A” (positive values) corresponding to euchromatin and “B” (negative values) corresponding to heterochromatin. The Fiedler vector and first principal component (PC1) vector are mathematically equivalent. However, unlike the PC1 vector, the Fiedler vector is accompanied by its corresponding Fiedler number which allows us to assign a magnitude of connectivity to a network. We characterize compartment switch events by identifying genomic bins with differing sign and magnitude above the 90th percentile of vector values between settings.

Identification of TADs

Topologically associating domains (TADs) were identified using spectral clustering as described in Chen et al. (2016). This technique calculates the Fiedler vector for a normalized Hi-C adjacency matrix and initially organizes neighboring regions whose Fiedler vector values have the same sign into shared domains. This initial TAD structure is repartitioned if for a given domain, the Fiedler number is less than a user-defined threshold (thr) to ensure that the TADs represent well-connected regions and are not too large. Resulting

TADs are iteratively repartitioned until their respective Fiedler numbers are larger than λ_{thr} or until the smallest allowable TAD size (default is 300 kb) is reached. We perform this procedure for chromosome level Hi-C contact maps pooled across samples at 50 kb resolution. For our analysis, λ_{thr} was chosen to ensure a median TAD size of 900 kb, as the expected median TAD size in mammalian genomes is 880 kb (rounded to 900 kb for our data since bins are in intervals of 50 kb) (Dixon et al., 2012; Bonev and Cavalli, 2016). A specific λ_{thr} was chosen for each chromosome and sample to ensure each TAD clustering set would have the same approximate median TAD size.

Quantifying internal TAD organization

The internal structure of TADs is comprised of transient interactions over varying lengths that form chromatin 'loops'. In the absence of WAPL, loop length increases, enriching contact frequency between either boundary of a given TAD (Haarhuis et al., 2017). Visually, we identify these interactions by the notable density of contacts present in the top right or bottom left corners of TADs. We quantify the strength of these interactions by designating a local neighborhood with a window size of 150 kb by 150 kb centered around the corner of each TAD. We then find the nonzero average of observed contacts in each window. TADs that are less than or equal to the window size are ignored (corner peak signal set to 0). This is performed for every TAD across each setting and chromosome. To evaluate the statistical significance of a given change in corner peak signal between WT and KO cells, we compared each corner peak signal to a background set of interactions. This background set is made up of contacts in the region between the diagonals encompassing the corner peak neighborhoods. We evaluate the p-value of each corner peak signal based on the proportion of background interactions with a signal less than the corner peak signal. As such, we determined that if a corner peak has a higher signal in the KO cells compared to WT cells and is significantly higher than interactions at comparable distances ($p < 0.01$), then the corner peak enrichment is statistically significant.

Hi-C derived 5C contact map generation

We constructed a synthetic 5C contact map derived from a genome-wide 1Mb Hi-C contact map for genomic regions containing genes in the cell cycle gene networks. This was done by locating the genomic bins corresponding to cell cycle genes, extracting the inter-chromosomal and cell cycle loci-specific intra-chromosomal interaction frequencies for those bins, and stitching them together in genomic order. Our working set of cell cycle genes was sourced from the KEGG database and included 170 genes distributed across all chromosomes in the genome. Some of the genes occupy the same 1Mb genomic bins resulting in a 141 by 141 dimension adjacency matrix at 1Mb-resolution.

Cell proliferation assay

CellTrace™Far Red was utilized for our cell proliferation assay. Purified T cells were labeled with far-red at a final concentration of 1 mol/L according to the manufacturer's instruction (Molecular Probes, C34564). Far Red-labeled T cells were cultured similarly to above MLR for allogeneic reaction or Dynabeads T cell activator CD3/CD28 stimulation for up to 7 days. Then, collected cells were examined with flow cytometry, gated for CD3 (APC) positive, and Far Red dilution was determined.

FxCycle™Far Red Stain for DNA content measurement

For *in vitro* experiments, WT or *Wapl* KO T cells were treated with Dynabeads T cell activator CD3/CD28 stimulation for up to 4 days. For *in vivo* experiments, transferred WT and *Wapl* KO T cells were isolated and purified from spleens of BALB/c recipient mice on day 7 after allogeneic BMT. The T cells were fixed with 10% formaldehyde for 30 min, washed 3 times with PBS and the sample cell concentration was adjusted at 1×10^6 cells/mL. FxCycle™ Far Red stain (200 nM) (Molecular Probes, F10348) and 5 L of RNase A (20 mg/mL) (Roche Cat. 70294823) were added to flow cytometry samples and continued for incubation at room temperature for 30 min and protected from light. Samples were analyzed with flow cytometer (AttuneNxT) without washing using 633 nm excitation and emission collected in a 660 bandpass. The DNA contents were determined as 2C and >2C by fluorescence intensities.

ELISA

Concentrations of TNF- α and IFN- γ in sera on day 21 after allogeneic BMT were measured with specific anti-mouse ELISA kits from BD Biosciences. Assays were performed per the manufacturer's protocol and read at 450 nm in a microplate reader (Bio-Rad). The concentrations were calculated from triplicate samples as mean \pm SEM.

FACS

Single-cell suspensions of spleens and thymii were prepared as previously described (Sun et al., 2015). Briefly, to analyze surface phenotype, purified T cells and thymocytes from B6 WT, *Wapl* KO deficiency mice, or transplanted animals, were washed with FACS wash buffer (2% bovine serum albumin [BSA] in phosphate-buffered saline [PBS]), pre-incubated with the rat anti-mouse FcR mAb 2.4G2 for 15 min at 4°C to block nonspecific FcR binding of labeled antibodies, then resuspended in FACS wash buffer and stained with conjugated monoclonal antibodies purchased from BD Biosciences (San Jose, CA): allophycocyanin (APC)-conjugated monoclonal antibodies (MoAbs) to CD4, CD8, CD3, CD45.2, CD45.1, CD25 and CD69; phycoerythrin (PE)-conjugated MoAbs to CD3, CD4, CD8, CD25, and TCR β ; allophycocyanin (APC)-conjugated MoAbs to CD3, CD4, and PerCP/Cy5.5-conjugated MoAbs to CD3, CD4 and CD8 were purchased from eBioscience (SanDiego, CA). Next, cells were analyzed using an AttuneNxT flow cytometer. For intracellular staining, cells were stained for CD4 and CD25 antibodies as above, then fixed with IC Fixation Buffer (Biolegend, Cat. No.420801) and incubated 20–60 min at room temperature and continued by adding 2 mL of 1X Permeabilization Buffer (Biolegend Cat. No. 421002) and centrifuged at 400–600 \times g for 5 min at room temperature. Cell pellets were resuspended in 100 L of 1X permeabilization buffer and PE-conjugated FoxP3 antibody (eBioscience, SanDiego, CA, Cat. 126403) was added at 0.5 ug/million cells/100 ul and incubated for 30 min at room temperature. Stained cells were resuspended in an appropriate volume of Flow Cytometry Staining Buffer for flow cytometry analyses. Apoptotic cells were detected by PE-Annexin V staining.

QUANTIFICATION AND STATISTICAL ANALYSIS

All quantifications were subjected to normal distribution analysis with the D'Agostino and Pearson normality test. Statistical p values for two-group comparison were conducted by a two tailed Student's t test for parametric distributions and a Mann-Whitney test for non-parametric results. For comparisons between more than two groups, p values were calculated using a one-way ANOVA with Dunnett's or Sidak's test for parametric distributions and a Kruskal Wallis test with Dunn's post hoc test for non-parametric distributions. Statistical analyses were performed in GraphPad Prism8 (GraphPad Software, San Diego, CA). Briefly, comparisons between two groups were calculated using a t-test, while comparisons between two groups at multiple time points were calculated using the Holm-Sidak method. A log-rank (Mantel-Cox) test was used to analyze all survival data. A Mann-Whitney test was used for the statistical analysis of clinical scores (Sun et al., 2015). Bar graphs and scatter graphs show the mean and standard error of the mean (SEM). For all statistical tests, p-values are denoted as follows. ****p < 0.0001; ***p < 0.001; **p < 0.01; *p < 0.05.